MSDE

ROYAL SOCIETY OF CHEMISTRY

REVIEW

View Article Online
View Journal | View Issue

Check for updates

Cite this: *Mol. Syst. Des. Eng.*, 2020, **5**, 1098

Synergistic computational and experimental discovery of novel magnetic materials

Balamurugan Balasubramanian, *[a] Masahiro Sakurai, [b] Cai-Zhuang Wang, [c] Xiaoshan Xu, [a] Kai-Ming Ho,[c] James R. Chelikowsky[bd] and David J. Sellmyer *[a]

Received 30th April 2020,
Accepted 3rd June 2020

DOI: 10.1039/d0me00050g

rsc.li/molecular-engineering

New magnetic materials for energy and information-processing applications are of paramount importance in view of significant global challenges in environmental and information security. The discovery and design of materials requires efficient computational and experimental approaches for high throughput and efficiency. When increasingly powerful computational techniques are combined with special non-equilibrium fabrication methods, the search can uncover metastable compounds with desired magnetic properties. Here we review recent results on novel Fe-, Co- and Mn-rich magnetic compounds with high magnetocrystalline anisotropy, saturation magnetization, and Curie temperature created by combining experiments, adaptive genetic algorithm searches, and advanced electronic-structure computational methods. We discuss structural and magnetic properties of such materials including Co– and/or Fe–X compounds (X = N, Si, Sn, Zr, Hf, Y, C, S, Ti, or Mn), and their prospects for practical applications.

Design, System, Application

The search for new magnetic compounds is important to satisfy an ever-increasing demand for magnets with a wide range of applications including spintronics, data storage, hybrid vehicles, wind and water turbines, home appliances, catalysis, and biomedicine. Successful searches for new magnets require efficient computational and experimental approaches for high throughput and efficiency. Our paper reviews recent computational methods for predicting new magnetic compounds by combining adaptive genetic algorithm searches and advanced electronic-structure calculations. These computational methods are combined with experimental searches which include special non-equilibrium fabrication methods that have uncovered novel Fe-, Co- and Mn-rich magnetic compounds with high magnetocrystalline anisotropies, saturation magnetizations, and Curie temperatures.

1. Introduction

The discovery and design of new complex materials with significant physical properties has been a central focus in science and technology for decades.[1–3] An example of recent discovery efforts include the Materials Genome Initiative.[4,5] Our focus centers on finding new magnetic materials as these materials play a crucial role in a wide range of applications such as spintronics, data storage, hybrid vehicles, wind and water turbines, home appliances including refrigeration and air conditioning, catalysis, and biomedicine.[6–10] The demand for magnets is rapidly growing owing to an increasing world population and modern technological requirements. Specifically, the search for novel magnetic materials targets magnets that are free of scarce and expensive elements and exhibit suitable magnetic properties. These properties include a high magnetocrystalline anisotropy (K_1, the energy required to deflect the magnetic moment in a crystal from the easy- to hard-axis direction), a large saturation magnetic polarization ($J_s = 4\pi M_s$ in cgs or $\mu_0 M_s$ in SI unit, where M_s is the saturation magnetization above which the magnetization cannot be increased by an applied magnetic field H), a high Curie temperature (T_c, a critical temperature above which a ferromagnetic material transforms into a paramagnet), a skyrmion (spin spiral or "twisted") spin structure associated with Dzyaloshinskii–Moriya interactions, a high spin polarization, a magnetic structure with zero or low net magnetization, and an improved magnetocaloric effect.

Our review of the discovery process is focused on the development of novel magnetic materials with high K_1, J_s, and T_c useful for information and energy technologies. Magnetocrystalline anisotropy is a key intrinsic property,

---

[a] Nebraska Center for Materials and Nanoscience and Department of Physics and Astronomy, University of Nebraska, Lincoln, Nebraska, 68588, USA.
E-mail: bbalasubramanian2@unl.edu, dsellmyer@unl.edu
[b] Center for Computational Materials, Oden Institute for Computational Engineering and Sciences, The University of Texas at Austin, Austin, Texas 78712, USA
[c] Ames Laboratory, U.S. Department of Energy and Department of Physics and Astronomy, Iowa State University, Ames, Iowa, 50011, USA
[d] McKetta Department of Chemical Engineering and Department of Physics, The University of Texas at Austin, Austin, Texas 78712, USA

Balamurugan Balasubramanian

Balamurugan Balasubramanian is a Research Assistant Professor in the Department of Physics and Astronomy and Nebraska Center for Materials and Nanoscience at the University of Nebraska-Lincoln. He received his M.Tech. in Solid State Materials and Ph. D. in Physics under the supervision of Prof. Bodh Raj Mehta from Indian Institute of Technology Delhi. His current research focuses on spin correlations in nanomagnets and novel magnetic materials for energy, spintronics, and quantum-information applications.

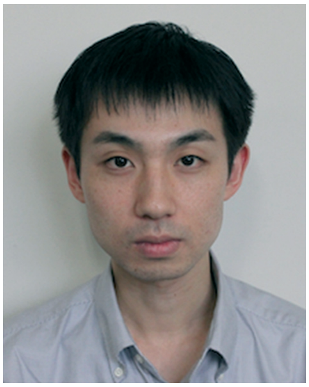

Masahiro Sakurai

Masahiro Sakurai received his D. Sc. in Condensed Matter Physics from Tokyo Institute of Technology in 2011. He was a postdoctoral fellow at the Institute of Solid State Physics, the University of Tokyo, before joining the Center for Computational Materials at the Oden Institute, the University of Texas at Austin in 2015. His research interests include first-principles calculations for the design and understanding of new magnetic materials.

Cai-Zhuang Wang

Cai-Zhuang Wang is a senior scientist at Ames Laboratory and an adjunct professor at Iowa State University. He received his PhD degree in condensed matter physics from International School for Advanced Studies (SISSA) in Trieste, Italy under the supervision of Professor Erio Tosatti and Professor Michael Parrinello. His research focuses on condensed matter theory and computational materials science.

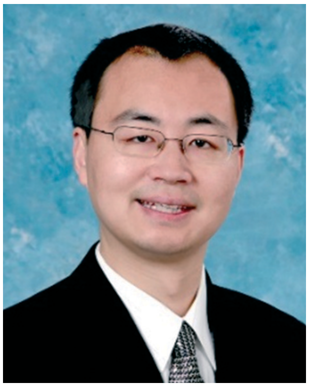

Xiaoshan Xu

Xiaoshan Xu is an Associate Professor in the Department of Physics and Astronomy at the University of Nebraska-Lincoln. He leads the Ferrothinfilm Lab, whose interests range from intermetallic compounds, complex oxides, to organic semiconductors, focusing on their ferroic properties.

James Chelikowsky

James Chelikowsky holds the W. A. "Tex" Moncrief Jr. Chair in Computational Materials within the Institute for Computational Engineering and Sciences at the University of Texas at Austin where he is a professor in the Departments of Physics, Chemical Engineering, and Chemistry, and director of the Center for Computational Materials. He received his B.S. in physics from Kansas State University and his Ph.D. in physics from the University of California at Berkeley. His research focuses on optical properties, interfacial phenomena, nano-regime systems, magnetic materials and the development of high performance algorithms to predict the properties of materials

David J. Sellmyer

David J. Sellmyer is George Holmes University Distinguished Professor in the Department of Physics and Astronomy at the University of Nebraska. He was founding director of the Nebraska Center for Materials and Nanoscience (1988-2019), Nebraska NSF Materials Research Science and Engineering Center (2002-2007), and NSF-National Nanotechnology Coordinated Infrastructure, Nebraska Nanoscale Facility (2015-2019). His research focuses on quantum and spin phenomena in nanomagnetic structures and he has (co-)authored and edited more than 700 research articles, chapters and reviews, and eight books. Sellmyer is a Fellow of the American Physical Society and American Association for the Advancement of Science.

which is essential for developing high coercivity (H_c) and energy product $(BH)_{max}$ in permanent magnets, and improve thermal stability of written bits in high-density recording media.[11–13] $(BH)_{max}$ is defined as the maximum of the product of B and H in the second quadrant of the BH curve, where $B = H + 4\pi M$ in cgs or $\mu_0(H + M)$ in SI unit is the flux density or magnetic-field induction, and H and M are the magnetic field and magnetization, respectively. Spin–orbit coupling and crystal-field interactions combine to create magnetocrystalline anisotropy, and rare-earth elements or expensive metals such as Pt are often required to achieve high K_1 in magnetic compounds.[14] For example, the widely used permanent magnets in traction motors and power generators contain Nd and Dy, which are critical materials owing to supply risk and price fluctuations.[15–17] Worldwide computational and experimental efforts exist to accelerate the development of new rare-earth-free magnetic compounds.[15,18–21]

The approach we describe for the discovery of new magnetic materials uniquely combines experiment, an adaptive genetic algorithm (AGA), and an electronic-structure method using density-functional theory (DFT) as schematically illustrated in the flowchart, Fig. 1. This approach provides an efficient pathway to uncover new magnetic compounds beyond the existing materials database, which may be significant for future technologies. AGA is a promising method to determine the crystal structures of unknown compounds based solely on chemical composition with a relatively rapid speed. This method does not require any assumptions on the Bravais lattice, atom basis, or unit-cell dimensions.[18] Second, non-equilibrium fabrication methods, such as high-pressure sputtering (or cluster deposition) and rapid quenching from the melt (or melt spinning), can produce metastable phases. These phases require very high formation temperatures and may represent entirely new compounds, which do not exist in the equilibrium phase diagram.[15,20,21] Finally, advanced DFT computational methods are useful to calculate intrinsic magnetic properties and quickly screen potential materials for further characterization and processing.

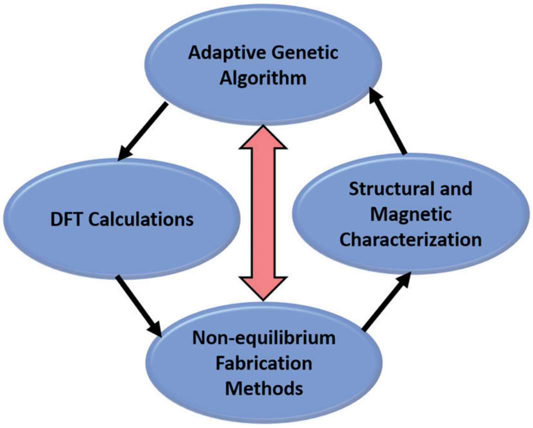

Fig. 1 Material search. A flow chart representing the development of new magnetic materials by combining computational and experimental methods.

Our review is organized as follows: section 2 begins with a summary of theoretical and computational methods including the adaptive genetic algorithm for ordered compounds and the density-functional theory approach for magnetic structures. This is followed by a description of two experimental methods for non-equilibrium fabrication of metastable phases: cluster deposition by high-pressure sputtering and rapid quenching from the melt at rates of order 10^6 K s^{-1}. In section 3 we discuss studies of several systems investigated by combined computational and experimental methods. Section 4 gives a brief overview of advances in and prospects for new rare-earth-free magnetic materials, and section 5 consists of concluding remarks and potential new directions.

2. Computational and experimental methods

2.1. Adaptive genetic algorithm

The AGA integrates the speed of classical interatomic potentials for structure-landscape exploration with an accuracy of first-principles theory for energy calculations. This approach enables the search for lower-energy structures of crystalline compounds with high efficiency and accuracy.[22,23] The flowchart of the AGA scheme consists of two main loops, a conventional genetic algorithm (GA) loop on the left and a novel adaptive loop on the right as illustrated in Fig. 2.

A GA mimics a Darwinian evolutionary process to solve challenging problems in crystal-structure prediction.[24] The initial pool of N_p trial structures at the beginning of the GA loop is randomly generated using the information of chemical composition of the compound to be sought. Supplementing space group-symmetry or lattice-vector information (if available from experiments) provides additional help to generate more relevant trial structures and enhance the performance of the GA search. During the GA optimization process, inheritance, mutation, and crossover operations are included to produce new off-spring structures. The most fit survivors are selected from generation to generation. While all GA implementations follow the same general strategy, a real space representation of the structure optimization and a geometrical cut-and-paste operation to generate off-spring structures from parent structures developed by Deaven and Ho have been demonstrated to be more efficient[24] and have been widely adapted.[22–33]

In practice, the numbers of parent structures N_p in the GA pool and the off-spring structures N_0 to be generated depend on the complexity of the investigated system. For most systems, the setting of N_p to about 4–6 times of the number of atoms in the unit-cell of the structure and N_0 to about twice of N_p has been found to be a reasonable choice. The unit cell length and type of the crystals can be either fixed or varied during the optimization of the structure. The total

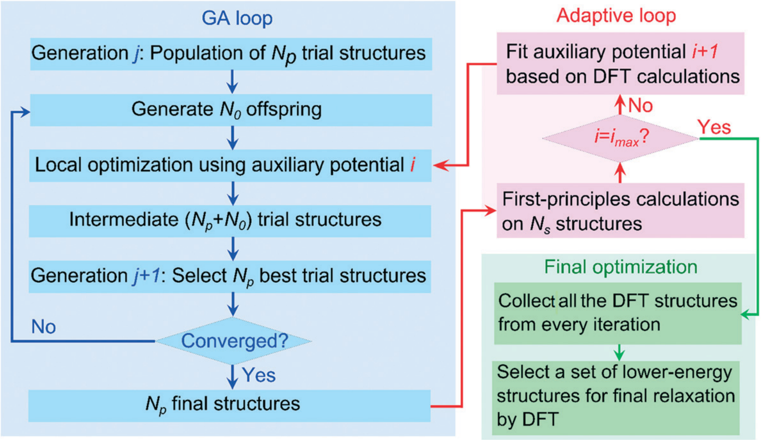

Fig. 2 Computational search process for new materials. A flowchart of the adaptive genetic algorithm (AGA) scheme.

energy of the system is commonly used as the fitness function for the survival during the GA process, although other properties of the materials can also be included in the fitness function.

The most time-consuming step in the GA loop is the local optimization for the new off-springs at every GA generation. During this step, the candidate structures are relaxed to the nearest local minima and their energies at the local minima are calculated in order to proceed to the survival selection and update the process. For complex structures, the GA search usually iterates over several hundreds or thousands of generations. Therefore, many structures need to be locally optimized. While first-principles calculations can give accurate results on the structures and energies, this approach is too expensive for such massive calculations. On the other hand, the structure relaxation and energy evaluation using empirical classical potentials can be much faster, but the accuracy of the predictions is questionable. The AGA scheme aims to overcome this discrepancy by incorporating an adaptive loop to the conventional GA loop to harness the advantages of both calculations in a very efficient way.

Within the AGA approach, the most time-consuming structural relaxation during the GA search is carried out using the less-expensive auxiliary classical potential, which is continually adjusted in the adaptive loop by fitting to the results from accurate DFT calculations on a small subset of "lower-energy" candidate structures predicted by the GA. At the same time, all the candidate structures calculated by methods using DFT from iteration to iteration are collected for final refinement to determine the global lower-energy structures. In this way, the auxiliary classical potential helps to efficiently explore the configuration space though the GA, and expensive DFT calculations are kept to the minimum without losing the efficiency and accuracy of the structure prediction. Note that the adaptive loop in the AGA scheme can be regarded as a machine learning (ML) loop. ML based interatomic potentials can be implemented during the search process. For rare-earth-free magnetic compounds presented in this review, the mathematical form of the embedded atom method is used for the auxiliary classical potential.[34] Energies, forces, and stresses from first-principles DFT calculations are used to update the parameters of the auxiliary classical potentials *e.g.*, by a force-matching method with a stochastic simulated annealing algorithm as implemented in the potfit code.[35,36]

2.2. Real-space formalism

First-principles calculations discussed in this review are mostly based on the density-functional theory (DFT)[37,38] combined with the pseudopotential approach.[39] Within the DFT, the many-electron problem is mapped onto an effective one-electron problem, and a generalized-gradient approximation (GGA) is adopted for the exchange–correlation functional.[40] In the pseudopotential approach, the all-electron potential is replaced by a weaker effective pseudopotential that reproduced the effects of the core electrons on the valence states, which allows replication of the valence wave functions outside of the ion core.

The Kohn–Sham equations are solved in real-space. Real-space numerical electronic-structure methods are mathematically robust, accurate and well suited for modern, massively parallel computing resources.[41] We use a uniform grid in real space as implemented in the PARSEC code.[41–43] The Laplacian operator in the kinetic-energy term is expanded by using a high-order finite-differencing scheme. Typically, a grid spacing of 0.3 a.u. (approximately 0.16 Å) is sufficient to achieve the convergence of the total energy to within 1 meV per atom for 3d transition-metal systems.[44–46]

The real-space method discussed in this review is specifically designed for nanoscale systems and also offers a number of advantages over plane-wave basis methods. For example, the real-space methods avoid the use of fast Fourier transforms (FFTs) altogether, leading to a substantial saving in global communications. Real-space methods do not require the use of a "supercell" for confined systems, such as nanoclusters. For example, a spherical domain as a boundary condition is employed to simulate the properties of an isolated cluster. The wave functions are sampled inside the domain and vanish beyond the domain boundary (typically 10 a.u. away from the outermost atom of a cluster).

An important feature of the real-space DFT code, PARSEC, is the use of advanced numerical algorithms to reduce the computational load. In particular, the Kohn–Sham equations are solved efficiently by using a subspace filtering technique that exploits Chebyshev polynomials.[47–49] This filtering algorithm helps to avoid explicit diagonalizations during the self-consistent field cycle. The filtering operations are robust and numerically efficient. More than an order of magnitude in the total computational time can be obtained when compared to conventional diagonalization-based methods.

For magnetic systems and spin–orbit effects, such as magnetocrystalline anisotropy, the standard Kohn–Sham equations are extended into the generalized 2 × 2 Kohn–Sham equations,[50,51] which include the noncollinear spin density, $m(r)$, as well as the relativistic effects arising from the spin–orbit interactions. More details of the real-space formalism for the generalized Kohn–Sham equations can be found elsewhere.[41,52,53]

2.3. Non-equilibrium fabrication methods

Fig. 3A shows a schematic of an inert-gas plasma condensation-type cluster-deposition method, which consists of two chambers, one for cluster formation and the other for deposition.[20,21] The cluster-formation chamber has a direct current (DC) magnetron plasma-sputtering discharge with a water-cooled gas-aggregation tube, where an elemental or composite target with desired stoichiometry is sputtered using a mixture of argon (Ar) and helium (He) to form nanoparticles. For the formation of oxide and nitride nanoparticles, oxygen or nitrogen gas is fed into the plasma region in the gas-aggregation chamber.[54,55] The nanoparticles are extracted as a collimated beam moving towards the deposition chamber for the deposition on substrates kept at room temperature. Prior to deposition, the easy-axis of single-crystal magnetic nanoparticles exhibiting high magnetocrystalline anisotropies can be aligned using an external magnetic field, and combined with a high magnetization soft phase to form exchange-coupled nanocomposite materials, if desired.[56–58]

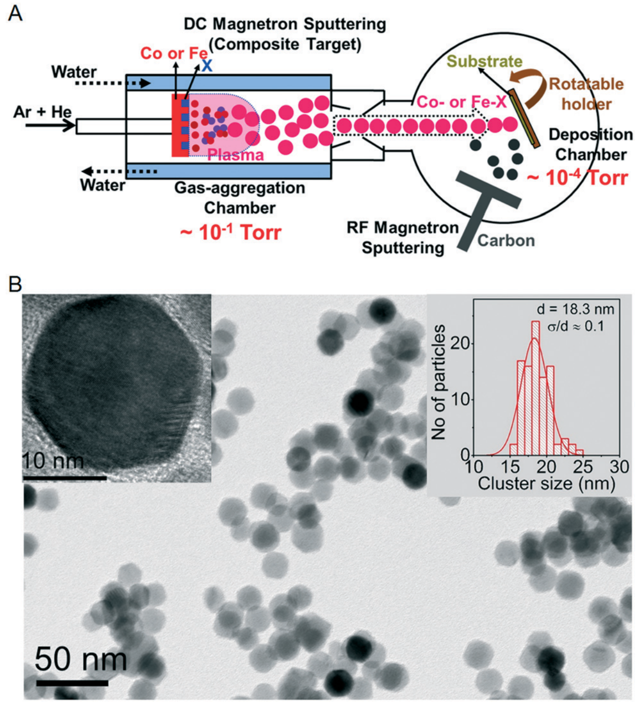

Fig. 3 Cluster-deposition process. (A) A schematic of the experimental set up. (B) Low-resolution TEM micrograph of Co_3Si nanoparticles, where the insets show a high-resolution TEM image of a single nanoparticle (left) and the particle-size histogram (right) revealing a narrow size-distribution (reproduced with permission from Balasubramanian *et al. Appl. Phys. Lett.* 2016, **108**, 152406. Copyright (2016) by the American Institute of Physics).

The crystal structure and average particle size in the range of 2–30 nm can be precisely tailored by controlling the gas-flow rates, deposition pressure, gas-aggregation length, and sputtering power. As an example, a transmission-electron-microscope (TEM) image of the cluster-deposited Co_3Si nanoparticles that form the $CdMg_3$-type hexagonal structure is shown in Fig. 3B.[59] The insets of Fig. 3B show faceting of a nanoparticle, typical for hexagonal crystal structures (left) and the particle-size histogram revealing a narrow size-distribution with an average particle size d = 18.3 nm and a standard deviation of $\sigma/d \approx 0.10$ (right). Note that Co_3Si is a high-temperature line compound in the phase diagram, which is stable only for a single composition (25 at% Si) and in a narrow temperature range of about 1190 to 1200 °C.[60,61] The uniqueness of the non-equilibrium cluster-deposition process has made the synthesis of this metastable compound possible.

Another method used for producing new and/or metastable magnetic compounds involves rapid quenching of molten alloys. For this, high-purity elements with appropriate amounts are melted using a conventional arc-melting process to prepare alloys having the desired composition. The arc-melted alloys are re-melted to a molten state in a quartz tube. They are subsequently ejected onto the surface of a water-cooled rotating copper wheel to form nanocrystalline ribbons of an approximate width of 2 mm and a thickness of 40 μm as schematically shown in Fig. 4A. The cooling rate is of order 10^6 K s^{-1}. Fig. 4B shows the nanostructure of a melt-spun $Co_{1.043}Si_{0.957}$ sample (left) and its annular bright-field (ABF) scanning-transmission-electron-microscopy (STEM) image revealing the atomic arrangements of Co and Si corresponding to the cubic B20 structure with the FeSi prototype and non-centrosymmetric $P2_13$ space group (right).[62] Note that the solid solubility of Co in CoSi is limited to $x \leq 0.02$ under equilibrium conditions, yielding alloys with the nominal composition $Co_{1.02}Si_{0.98}$.[60,61] Recent results indicate that a non-equilibrium process can also extend the solubility region in the phase diagram.[62]

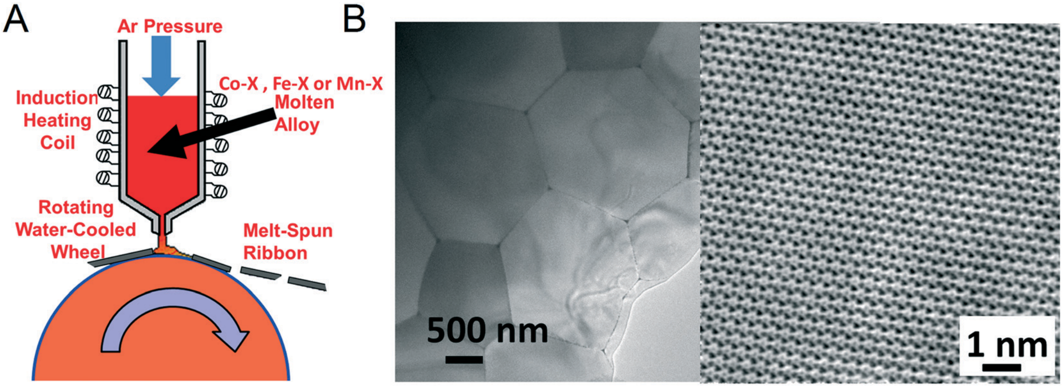

Fig. 4 Melt-spinning method. (A) A schematic of the process. (B) Low-resolution TEM micrograph (left) and annular bright-field scanning transmission-electron microscope image (right) for a melt-spun $Co_{1.043}Si_{0.957}$ ribbon (reproduced with permission from Balasubramanian *et al. Phys. Rev. Lett.* 2020, **124**, 057201. Copyright (2020) by the American Physical Society).

3. Studies of novel compounds

The focus of this review is on new stable and/or metastable Co- and/or Fe-rich transition-metal compounds crystallizing in non-cubic crystal structures, which have high potential to exhibit large K_1, J_s, and T_c values. Transition metals, such as Ti, Hf, Zr, Y, and Sn, combined with Co and/or Fe to form non-cubic structures might play a similar role to Pt and rare-earth elements in creating high magnetocrystalline anisotropy. Another approach is to create structures by incorporating gas elements such as nitrogen in the interstitial and substitutional sites of Fe and Co and by combining Fe and Co with metalloid elements such as C, Si, and S.

3.1. New interstitial and substitutional-type Co–N compounds

Examples of newly discovered materials using combined computational and experimental methods are the recently developed Co–N compounds.[46,55,63] The AGA search predicted a significant number of new cobalt–nitride compounds as opposed to a few existing equilibrium phases in the Co–N binary phase diagram and reported by earlier studies.[64–67] The new Co–N structures were created by incorporating the nitrogen atoms in the interstitial or substitutional occupancies of hcp Co, and the calculated formation energies for most of the compounds, Fig. 5A, are comparable with those of previously synthesized Co–N structures.[63] The AGA search subsequently has assisted the synthesis of a set of new high-anisotropy Co_3N compounds, such as interstitial-type rhombohedral (Fig. 5B) and substitutional $CdMg_3$-type hexagonal (Fig. 5C) structures, in the form of nanoparticles using the cluster-deposition method.[55] Fig. 5D shows good agreement with the experimental X-ray diffraction (XRD) patterns of the Co_3N nanoparticles with the corresponding simulated XRD patterns using the new rhombohedral and hexagonal-type Co_3N structures. The Rietveld refinement analysis shows a = 5.042 Å and c = 4.090 Å (hexagonal phase) and a = 4.611 Å and c = 13.062 Å (rhombohedral).[55]

The total densities of states calculated using DFT reveal that the hexagonal and rhombohedral Co_3N are ferromagnetic as shown in Fig. 6A and B, respectively. The corresponding densities of states clearly show that the rhombohedral compound is a weak ferromagnet (Fig. 6A), with holes in both the ↑ and ↓ bands and the hexagonal compound is a strong ferromagnet, with essentially a fully occupied ↑ band (Fig. 6B).[46,55] The calculated saturation

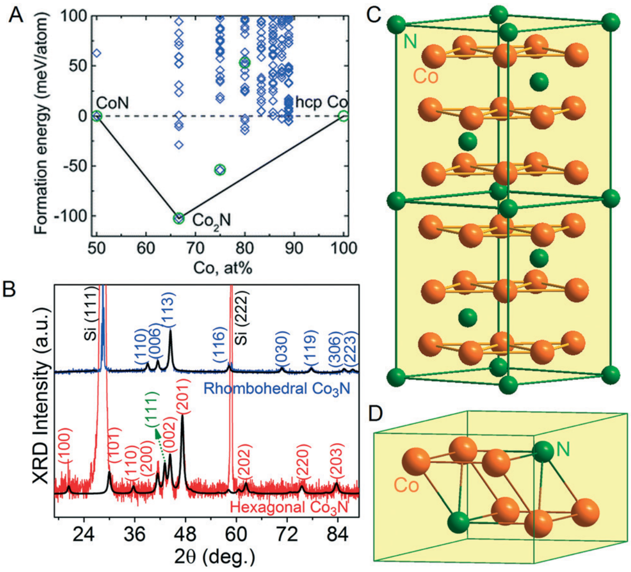

Fig. 5 Cobalt nitride compounds. (A) Formation energies calculated using the energies of CoN and hcp Co as references. Green circles and blue diamonds represent already reported experimental phases and new compounds predicted using the AGA, respectively (reproduced from ref. 63 with permission from The Royal Society of Chemistry). Schematic of the new Co_3N structures: (B) rhombohedral and (C) $CdMg_3$-type hexagonal. (D) The experimental XRD patterns measured using a Cu K_α wavelength of about 1.54 Å for the hexagonal Co_3N (red) and rhombohedral Co_3N (blue) nanoparticles are fitted with the corresponding structures using Rietveld analysis (black curve) (reproduced from ref. 55 with permission from The Royal Society of Chemistry). A minor (111) XRD peak is observed in the hexagonal nanoparticles due to the presence of about 3% of fcc Co.

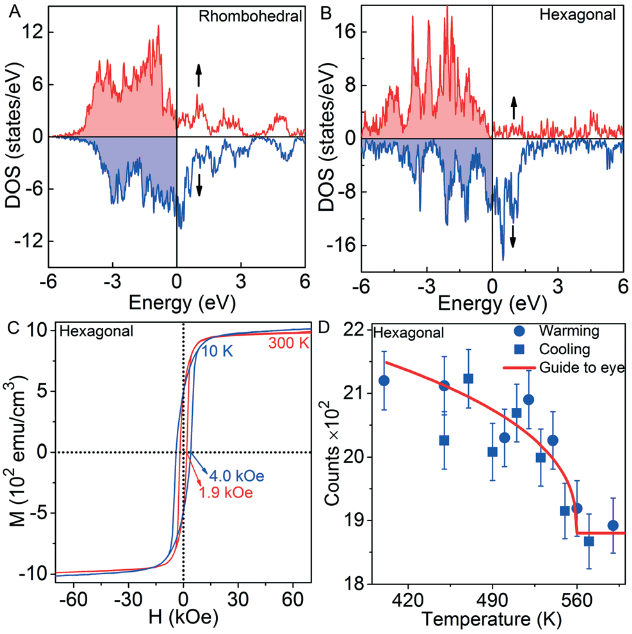

Fig. 6 Magnetic properties of Co$_3$N. (A) and (B) Total densities of states for bulk rhombohedral and hexagonal structures, respectively. (C) Field-dependent magnetization curves measured at 300 K and 10 K for the hexagonal nanoparticles. (D) Neutron diffraction intensity of the (002) peak for the easy-axis aligned hexagonal nanoparticle film. A transition between 500 K and 600 K was observed for both warming (circle) and cooling (square) curves, whereas the red line is a guide to the eye (reproduced from ref. 55 with permission from The Royal Society of Chemistry).

magnetizations of the bulk rhombohedral and hexagonal Co$_3$N structures are 662 emu cm^{-3} (or J_s = 8.3 kG) and 1198 emu cm^{-3} (or J_s = 15.1 kG), respectively, in fair agreement with the corresponding experimental values J_s = 7.3 kG (rhombohedral) and 12.8 kG (hexagonal).

The rhombohedral and hexagonal Co$_3$N compounds also exhibit significant magnetocrystalline anisotropy as evident from their field-dependent magnetization (M–H) curves. For example, the hysteresis loops of the hexagonal Co$_3$N compound show appreciable coercivities of 1.9 kOe at 300 K and 4 kOe at 10 K (Fig. 6C). The measured magnetic anisotropies and Curie temperatures are significant for the rhombohedral (K_1 = 10.4 Mergs per cm^3 and $T_c \approx 440$ K) and hexagonal Co$_3$N (K_1 = 10.1 Mergs per cm^3 and 550 K).[55] Fig. 6D shows the temperature dependence of the (002) diffraction intensity for the hexagonal Co$_3$N compound and reveals a clear magnetic transition between 500 K and 600 K.

The magnitude of the total magnetic moments in Co$_3$N clusters with two different structural motifs was explained well by means of density-of-states analysis. Real-space DFT calculations found that the total magnetic moment of Co$_3$N clusters can be controlled by the amount of nitrogen.[46] As shown in Fig. 7, there is an increasing trend in the total magnetic moment for a wide range of N concentrations in hexagonal Co$_3$N$_{1+x}$ clusters having $P63/mmc$ local atomic coordination. In particular, the total magnetic moment can be maximized with an optimal composition of about Co$_3$N$_{1.1}$.

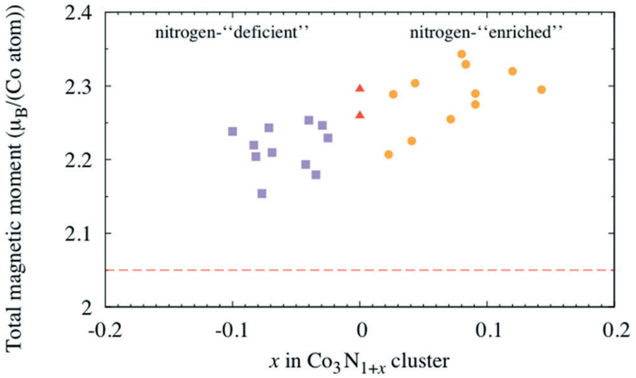

Fig. 7 Magnetism of the hexagonal Co$_3$N$_{1+x}$ clusters. Total magnetic moments of clusters containing 50–100 Co atoms with different nitrogen contents. The red dashed line indicates the magnetic moment of $P6_3/mmc$ Co$_3$N bulk, 2.05μ_B per atom, neglecting the orbital moments (reproduced with permission from Sakurai *et al. Phys. Rev. Mater.* 2018, **2**, 024401. Copyright (2018) by the American Physical Society).

3.2. Magnetic compounds with easy-plane anisotropies

A combination of experimental and theoretical research recently discovered magnetic compounds with high easy-plane anisotropies such as Co$_3$Si and Fe$_3$Sn.[59,68] Co$_3$Si is an intriguing material, which was predicted to crystallize in the CdMg$_3$-type hexagonal structure with lattice parameters a = 4.976 Å and c = 4.069 Å (space group: $P6_3/mmc$).[61] In addition to the equilibrium Co–Si phases in the phase diagram,[60] the AGA search found a new orthorhombic Co$_3$Si compound with lattice parameters a = 6.26 Å, b = 7.42 Å, and c = 3.69 Å and a space group *Cmcm*.[69] The convex hull diagram for Co–Si, Fig. 8A, shows that the orthorhombic Co$_3$Si has lower formation energy than hexagonal Co$_3$Si and higher than those of previously reported structures such as Co$_2$Si, CoSi and CoSi$_2$.[69] The non-equilibrium cluster-deposition method has produced Co$_3$Si nanoparticles and the Rietveld fitting of the experimental XRD pattern confirms the formation of the CdMg$_3$-type hexagonal structure (Fig. 8B).[59] The nanoparticles exhibit an increase in lattice parameters a = 4.990 Å and c = 4.497 Å as compared to the corresponding bulk values (a = 4.976 Å and c = 4.069 Å).[61,69]

The total density of states for nanoparticles, Fig. 8C, show a saturation magnetic polarization of 9.6 kG (1.34μ_B per Co), slightly higher than the theoretical bulk magnetic polarization of 9.2 kG (1.28μ_B per Co).[59] This difference can be attributed to the reduced coordination number of the Co atoms near the surface, which enhances the magnetization of atoms at the particle surface. The DFT calculations also show that hexagonal and orthorhombic Co$_3$Si phases have easy-plane anisotropies with $K_1 \approx -5.2$ and -64 Merg per cm^3, respectively.[59,69]

The magnitude of K_1 for the hexagonal Co$_3$Si is comparable with that of L1$_0$-ordered FePt and much higher than that of other rare-earth-free permanent-magnet materials.[15] We note that negative anisotropy generally leads

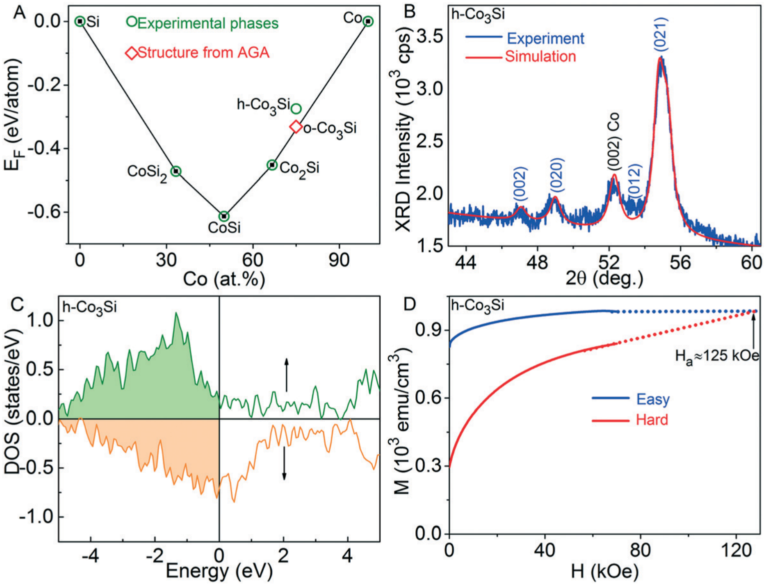

Fig. 8 Co–Si compounds. (A) Formation energy convex hull calculated using the energies of the hcp Co and diamond Si as references (reproduced with permission from Zhao *et al. Phys. Rev. B* 2017, **96**, 024422. Copyright (2017) by the American Physical Society). (B) Experimental XRD pattern of Co_3Si nanoparticles measured using a Co K_α wavelength of about 1.7789 Å is compared with the simulated X-ray diffraction patterns using the $CdMg_3$-type hexagonal structure. A minor (002) reflection corresponding to hcp Co is also observed. (C) Total density of states calculated for a Co_3Si nanoparticle having 64 atoms. (D) Field-dependent magnetization curves measured at 10 K along the easy- and hard-axis for an aligned Co_3Si nanoparticle film. The anisotropy field H_a (indicated by an arrow) is evaluated by extending the experimental easy- and hard-axis magnetization curves (dotted line) to intersect (reproduced with permission from Balasubramanian *et al. Appl. Phys. Lett.* 2016, **108**, 152406. Copyright (2016) by the American Institute of Physics).

to negligibly low coercivities in bulk crystals, but the hexagonal Co_3Si nanoparticles exhibit high coercivities (17.4 kOe at 10 K and 4.3 kOe at 300 K). This result is a consequence of the exchange coupling between the nanoparticles, which creates an effective easy axis.[59,70] Fig. 8D shows the low-temperature magnetization curves of the aligned Co_3Si nanoparticles measured along the easy and hard axes, which reveal a high anisotropy field H_a of about 125 kOe, corresponding to an effective anisotropy constant K_{eff} = 48 Mergs per cm^3. Similarly, Fe_3Sn forms a Ni_2In-type hexagonal structure with a = 5.46 Å and c = 3.35 Å, and shows an easy-plane anisotropy K_1 = −18 Mergs per cm^3, J_s = 14.8 kG, and T_c = 725 K.[68] DFT calculations and experiments also revealed that the alloying with a third element such as Sb can alter the anisotropy from the easy plane (−ve K_1) in Fe_3Sn to the easy axis (+ve K_1) in $Fe_3Sn_{0.75}Sb_{0.25}$.[68,71]

3.3. Fe_3Co_2Ti-Based compounds

A combination of AGA search, DFT calculations, and experiment has led to the discovery of a set of Fe- and Co-rich compounds $Fe_{3+x}Co_{3-x}Ti_2$ ($0 \leq x \geq 3$), which form a hexagonal structure with a $P\bar{6}m2$ symmetry.[72–75] The basic $Fe_3Co_3Ti_2$ structure is schematically shown in Fig. 9A and exhibits a significant Fe/Co anti-site mixing or disorder. Fig. 9B shows the neutron powder diffraction (NPD) spectrum measured at 10 K (open circles) and a fitted curve using the Rietveld method for the $Fe_3Co_3Ti_2$ alloy based on the $P\bar{6}m2$ hexagonal structure.[73] The best fit indicated a significant Fe/Co antisite disorder and also yielded the lattice parameters a = 4.743 Å and c = 15.444 Å for $Fe_3Co_3Ti_2$. Substitution of Fe

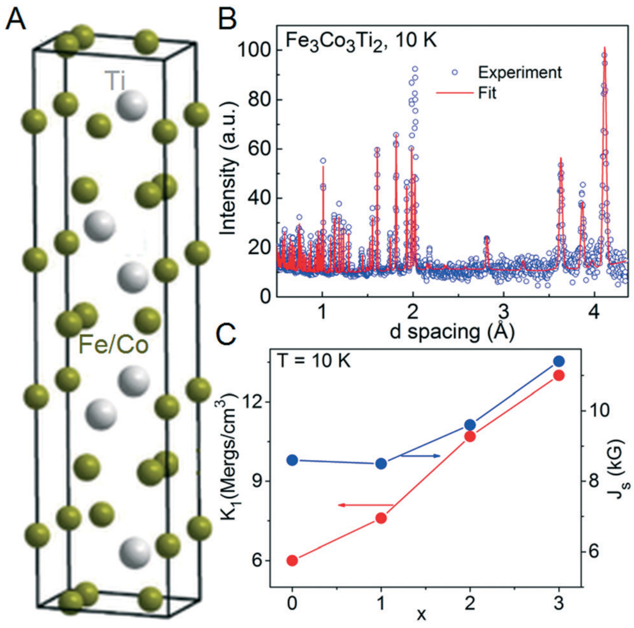

Fig. 9 Structure and magnetism of $Fe_{3+x}Co_{3-x}Ti_2$ compounds. (A) Unit cell for the parent compound (x = 0). (B) Neutron powder diffraction pattern for the x = 0 alloy measured at 10 K (circles) and the Rietveld fit (line) using the hexagonal $P\bar{6}m2$ structure. (C) Experimental K_1 and J_s values at 10 K (reproduced from Balasubramanian *et al. APL Mat.* 2016, **4**, 116109).

atoms for Co in the $Fe_3Co_3Ti_2$ lattice led to the formation of $Fe_4Co_2Ti_2$, Fe_5CoTi, and Fe_6Ti_2 with the same $P\bar{6}m2$ hexagonal structure, and magnetic properties such as K_1 and J_s significantly improved as shown in Fig. 9C.

A high magnetic anisotropy (13.0 Mergs per cm^3) and saturation magnetic polarization (11.4 kG) were measured at 10 K for the Fe_6Ti_2 compound,[73] and further NPD analysis shows that Fe substitution for Co in $Fe_{3+x}Co_{3-x}Ti_2$ decreases Fe/Co occupancy disorder and improves the magnetic properties including the uniaxial character of the magnetic anisotropy.[75] The projection of the magnetic moments with respect to the crystalline c axis at 100 K is shown as a function of x in Fig. 10A. The average angle between the magnetic moment and c axis decreases significantly with increasing Fe content, which may be due to the improved chemical ordering. The magnetization also improves on increasing Fe content in $Fe_{3+x}Co_{3-x}Ti_2$ as shown by NPD and magnetometry measurements (Fig. 10B), but T_c decreases slightly from 586 K ($Fe_3Co_3Ti_2$) to 513 K (Fe_6Ti_2).[75]

3.4. High-anisotropy Zr_2Co_{11} and $HfCo_7$ compounds

Zr_2Co_{11} has been extensively studied as a promising rare-earth-free permanent-magnet material due to its high K_1 = 13.5 Mergs per cm^3, J_s = 9.7 kG, and T_c = 783 K.[21,57] However, a complete crystal structure with atomic arrangements (Wyckoff positions) for Zr_2Co_{11} has been elusive for many years, and several complex crystal structures of the orthorhombic, rhombohedral, and hexagonal polymorphs have been shown to form near the Zr_2Co_{11} stoichiometry.[76,77] Recently, a systematic crystal structure search for $ZrCo_{5+x}$ compounds with $0 \leq x \leq 0.5$ has been carried out using the AGA search, which solved the atomic structure for Zr_2Co_{11}.[78]

Fig. 11A shows the convex hull of formation energies for various phases in a Zr–Co system with a stoichiometry close to Zr_2Co_{11}. Among these phases, the rhombohedral and orthorhombic structures have been synthesized using non-equilibrium melt-spinning and/or cluster-deposition methods.[21,57,76–78] For example, Fig. 11B and C show a schematic for the atomic structure of the rhombohedral phase (space group: $R32$, a = 4.69 Å and c = 24.0 Å) and a high-resolution transmission electron microscopy (HRTEM) image of a melt-spun Zr_2Co_{11} sample measured along the [010] zone axis, respectively.[78]

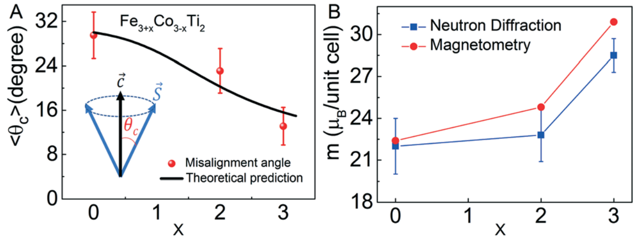

Fig. 10 Magnetic moment as a function of x in $Fe_{3+x}Co_{3-x}Ti_2$. (A) Misalignment angle with respect to c-axis measured using neutron powder diffraction at 100 K. The line is a theoretical prediction (see the ref. 75 for details). (B) Magnitude measured using magnetometry at 10 K and neutron diffraction at 100 K (reproduced with permission from Wang *et al. Phys. Rev. Mat.* 2019, **3**, 064403. Copyright (2019) by the American Physical Society).

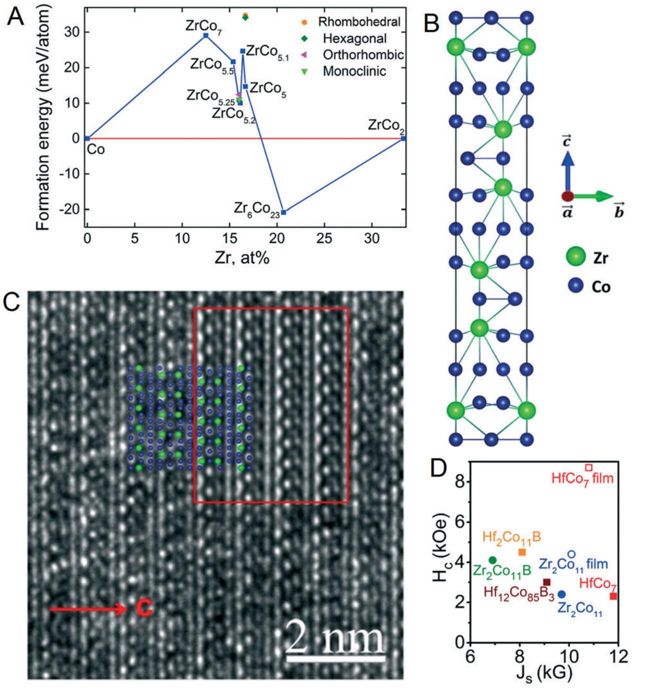

Fig. 11 Structure and magnetism of Zr–Co and Hf–Co systems. (A) Convex hull of formation energies for Zr–Co compounds and structures close to Zr_2Co_{11} stoichiometry. (B) Atomic structure proposed for the rhombohedral phase using AGA search. (C) High resolution TEM (HRTEM) image measured along the [010] zone axis. The red arrow indicates the repeated distance along the c axis. Inset within the red box is the simulated HREM image, and the structure model along the c axis is laid on top of the experimental HRTEM image (reproduced with permission from Zhao *et al. Phys. Rev. Lett.* 2014, **112**, 045502. Copyright (2014) by the American Physical Society). (D) The measured H_c and J_s values for melt-spun bulk alloys (solid symbols) and cluster-assembled nanostructured films (open symbols) [data were taken from Balasubramanian *et al. J. Phys. Condens. Mater.* 2014, **26**, 064204 ($HfCo_7$ and Zr_2Co_{11}), *Adv. Mater.* 2013, **25**, 6090 (Zr_2Co_{11} film), and *Sci. Rep.* 2015, **4**, 6265 ($HfCo_7$ film), McGuire *et al. Appl. Phys. Lett.* 2012, **101**, 202401 ($Hf_2Co_{11}B$), Chang *et al. Appl. Phys. Lett.* 2014, **105**, 192404 ($Hf_{12}Co_{85}B_3$) and Chen *et al. J. Appl. Phys.* 2005, 97, 10F307 ($Zr_2Co_{11}B$)].

The repeat distance along the c-axis in the HRTEM image is about 24.2 Å, nearly equal to the theoretically predicted lattice parameter c = 24 Å. In addition, the inserted structural projection and simulated atomic arrangements (red box) corresponding to the rhombohedral phase show good agreement with the measured HRTEM image (Fig. 11C). Similarly, a Co-rich Hf–Co compound close to the $HfCo_7$ stoichiometry having an orthorhombic structure, formed by cluster-deposition and melt-spinning methods, has shown a high $K_1 \approx$ 19.4 Mergs per cm^3, J_s = 11.8 kG and T_c = 751 K.[21,56,58] The AGA search and DFT calculations have also assisted in understanding the crystal structure and intrinsic magnetic properties of the $HfCo_7$ compound.[79,80]

In agreement with the experiment, DFT calculations show high magnetocrystalline anisotropy in the bulk alloys of rhombohedral Zr_2Co_{11} (K_1 = 14.2 Mergs per cm^3 and J_s = 10.9 kG) and orthorhombic Hf–Co (K_1 = 18.5 Mergs per cm^3 and J_s = 11.4 kG).[21,56–58,78–80] The underlying magnetic anisotropies have led to appreciable H_c and J_s values in the melt-spun Zr_2Co_{11} and Hf–Co alloys as shown in Fig. 11D.[21,80–86] The saturation magnetic polarization of these bulk alloys decreases upon alloying with boron, but H_c increases significantly (Fig. 11D), and this subsequently improves their energy products as discussed in section 4. On the other hand, the cluster-deposited nanostructured Hf–Co and Zr–Co films exhibit significant H_c as well as J_s as shown in Fig. 11D.

3.5. Novel MnBi-based magnetic materials

MnBi, which crystallizes in the hexagonal NiAs structure (space group $P6_3/mmc$), as shown in Fig. 12A, has long been considered as a potential permanent-magnet material along with other rare-earth-free materials. Bulk MnBi contains neither rare earths nor expensive elements and shows appreciable $J_s \approx 8.5$ kG and T_c = 650 K; it has a room-temperature magnetocrystalline anisotropy of 12 Mergs per cm^3 and exhibits an unusual increase of magnetic anisotropy with increasing temperature.[87–89] Sakuma *et al.* have predicted based on density-functional calculations that a replacement of Bi with a third element such as Sn increases the anisotropy of MnBi.[90] The non-magnetic Bi and Sn affect the magnetic anisotropy of the Mn sublattice through crystal-field or 'ligand-field' interactions. Since Sn has one fewer valence electrons than Bi, this leads to a slight reduction in magnetization.

Following theoretical predictions,[90] there were significant experimental studies on alloying MnBi with Sn, Sb, and Mg.[91–94] As predicted by DFT calculations, an easy-axis aligned melt-spun $Mn_{50}Bi_{45}Sn_5$ alloy has shown a significantly improved room-temperature anisotropy constant (20 Mergs per cm^3) as compared to that of an aligned MnBi sample (12 Mergs per cm^3).[91,94] This improvement was also reflected in the experimentally measured coercivities in the MnBi-based alloys (Fig. 12B) and their energy products as discussed in section 4.

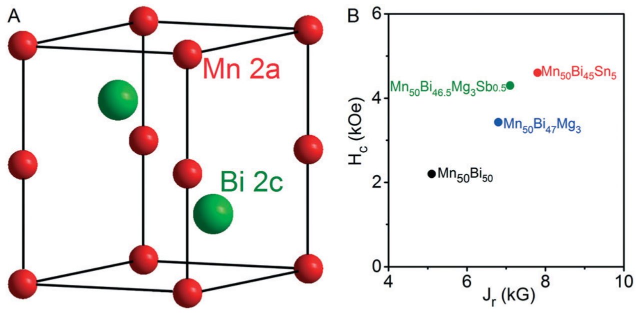

Fig. 12 Structure and magnetism of MnBi-based alloys. (A) Unit cell of MnBi (from ref. 94). (B) A combination of best coercivities and remanent magnetic polarizations ($J_r = 4\pi M_r$, where M_r is the remanent magnetization or M at H = 0 in the demagnetization M–H loops) obtained in the MnBi-based melt-spun ternary alloys [data were taken from Gabay *et al. J. Alloy Compounds* 2019, **792**, 77 and *J. Magn. Mag. Mater.* 2020, **495**, 165860 ($Mn_{50}Bi_{50}$, $Mn_{50}Bi_{46.5}Mg_3Sb_{0.5}$, $Mn_{50}Bi_{47}Mg_3$) and Zhang *et al. APL Mater.* 2019, **7**, 121111($Mn_{50}Bi_{45}Sn_5$)].

3.6. High-anisotropy metastable iron–cobalt nitrides

In addition to the experimentally observed hexagonal and rhombohedral Co_3N compounds, several metastable structures of other binary cobalt nitrides and ternary iron–cobalt nitrides with promising permanent-magnet properties were theoretically predicted.[63,95,96] For this, low-energy crystal structures of Co_nN compounds with n = 1, 2–8 were searched by the AGA, and a significant number of new structures of Co_nN (n = 3–8) were found to have lower energies than those previously discovered by experiments.[63] Some structures exhibit large magnetic anisotropy energy, reaching as high as 200 μeV per Co atom (or 24.5 Mergs per cm^3) based on first-principles density functional calculations as shown in Fig. 13. Substitution of some Co with Fe has also been observed to stabilize new structures with improved magnetic properties.[63]

Similarly, the structures and magnetic properties of ternary $Fe_{16-x}Co_xN_2$ ($0 \le x \le 16$) alloys were investigated using AGA and first-principles calculations.[95] Among the rare-earth-free magnets, the metastable tetragonal α''-$Fe_{16}N_2$ phase of iron nitrides has attracted considerable experimental and theoretical attention due to the low cost of Fe and high magnetization observed in the case of α''-$Fe_{16}N_2$ thin films.[3] It has been theoretically predicted that the replacement of Fe by Co in $Fe_{16}N_2$ improves the magnetic anisotropy of the material for a Co/Fe atomic ratio ≤1 as shown in Fig. 14.[95] The calculated magnetocrystalline anisotropy constant reaches 31.8 Mergs per cm^3 for $Fe_{12}Co_4N_2$, much larger than that of $Fe_{16}N_2$. From a systematic crystal-structure search, a structural transition from tetragonal $Fe_{16}N_2$ to cubic $Co_{16}N_2$ was observed in Co-rich compounds ($x > 8$). This result can be explained by electron counting analysis. The difference in magnetic properties between the Fe-rich ($x \le 8$) and Co-rich ($x > 8$) nitride compounds, shown in Fig. 14, is also closely related to the structural transition.[95]

3.7. Structure and magnetic properties of Co- and/or Fe-rich carbides and sulfides

Fe- and/or Co-rich carbide and sulfide alloys with different compositions have been investigated theoretically and experimentally to discover suitable magnetic compounds with high anisotropy and high magnetization.[15,97–100] Besides reproducing the known Fe_3C compound with a cementite (*Pnma*) structure, the AGA search also has captured several new metastable phases.[99] In particular, a bainite ($P6_322$) structure exhibits the largest magnetic moment among all the structures in the Fe_3C pool and its energy is only 4 meV higher than the low-energy cementite (*Pnma*) phase. Appreciable magnetocrystalline anisotropies, around 10 Mergs per cm^3, have

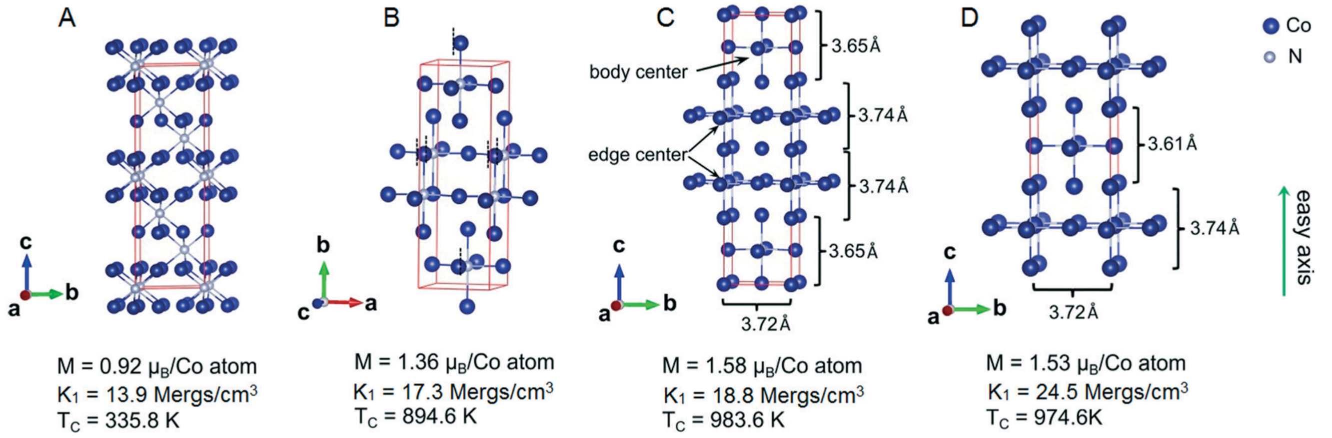

Fig. 13 Crystal structures of cobalt nitrides with large magnetocrystalline anisotropies. (A) Co_3N (space group *R*$\bar{3}$*c*), (B) Co_3N (space group *Cmcm*), (C) Co_4N (space group *I*4/*mmm*), and (D) Co_4N (space group *I*4/*mmm*) (reproduced from ref. 63 with permission from The Royal Society of Chemistry).

been measured in some metastable carbide phases including Fe_2CoC.[98,99] In addition, the AGA helped to identify the atomic structural model of the *Pnma* phase for Fe_2CoC, schematically shown in Fig. 15A, and the simulated XRD pattern based on the theoretical structural model is in good agreement with the experimental data as shown in Fig. 15B.[99]

The AGA has predicted new Fe_3S structures with formation energies lower than that of the experimentally reported *Pnma* structure as shown in Fig. 16A.[100] These low-energy structures can be classified into column-motif and layer-motif structures as schematically shown in Fig. 16B and C, respectively. Fe atoms are self-assembled into rods with a bcc-like lattice separated by the holes surrounded by S atoms in the column-motif structures (Fig. 16B). On the other hand, the bulk bcc Fe is broken into slabs of several layers and passivated by S atoms in the layer-motif structures (Fig. 16C). DFT calculations demonstrate that the column-motif Fe_3S structures exhibit reasonably high uniaxial magnetic anisotropy owing to the morphology of magnetic rod arrays. The replacement of Fe with Co further improves its magnitude.[100] We propose a follow-up investigation of this system with large unit cells to explore if larger Fe rods can be obtained and separated by large holes.

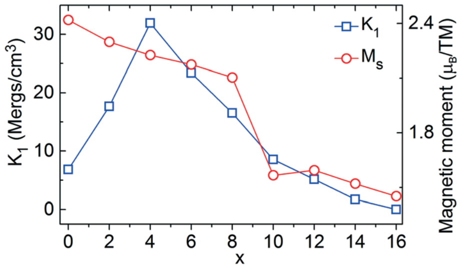

Fig. 14 Magnetic properties of $Fe_{16-x}Co_xN_2$. Magnetocrystalline anisotropy constant and magnetic moment per transition metal atom as a function of *x* (reproduced with permission from Zhao *et al. Phys. Rev.* B 2016, **94**, 224424. Copyright (2016) by the American Physical Society).

3.8. Magnetic properties of YCo_5 and $ZrCo_5$

A real-space pseudopotential formalism has successfully calculated the magnetocrystalline anisotropies in YCo_5 and $ZrCo_5$ compounds with five possible crystal structures in a hexagonal crystal family, schematically shown in Fig. 17.[101] These structures include all of the XCo_5 structures (X represents any other element) available in the literature including the experimentally observed structures.[21,78,102–104] The lattice constant and atomic positions of these structures are available in the Magnetic Materials Database.[105]

The magnetic anisotropy energy, E_a, the total-energy difference between the systems, where its magnetic moments, m, are oriented along the easy and hard axes, was computed using $E_a = E(m \perp c) - E(m \parallel c)$. Here, the easy (hard) axis is assumed to be along (perpendicular to) the crystallographic c axis. The magnetic anisotropy constant was then obtained using $K_1 = E_a/V$, where V denotes the volume of the system. Numerical details, such as the core radii of norm-conserving pseudopotentials, can be found in ref. 101.

Fig. 18 shows the magnetocrystalline anisotropy constant K_1 and the saturation magnetic polarization saturation J_s for YCo_5 and $ZrCo_5$ compounds. It was observed that YCo_5 and $ZrCo_5$ compounds can provide a moderate magnetic anisotropy constant ($K_1 \geq 10$ Mergs per cm^3) and a reasonable saturation magnetic polarization ($J_s \geq 10$ kG). These numbers are much better than those of conventional ferrite magnets, which account for one third of the total sales of the worldwide permanent-magnet market.[6] YCo_5 and $ZrCo_5$ compounds are free of heavy rare-earth and expensive elements leading one to speculate whether modified (alloyed) versions of these compounds may have potential for use in permanent-magnet applications.

3.9. Mn-Doped FeCo nanoclusters

Magnetism of transition-metal nanoclusters often deviates significantly from bulk owing to the reduced coordination number of surface atoms[106,107] and such nanostructures exhibit possible lattice relaxations or reconstructions at a

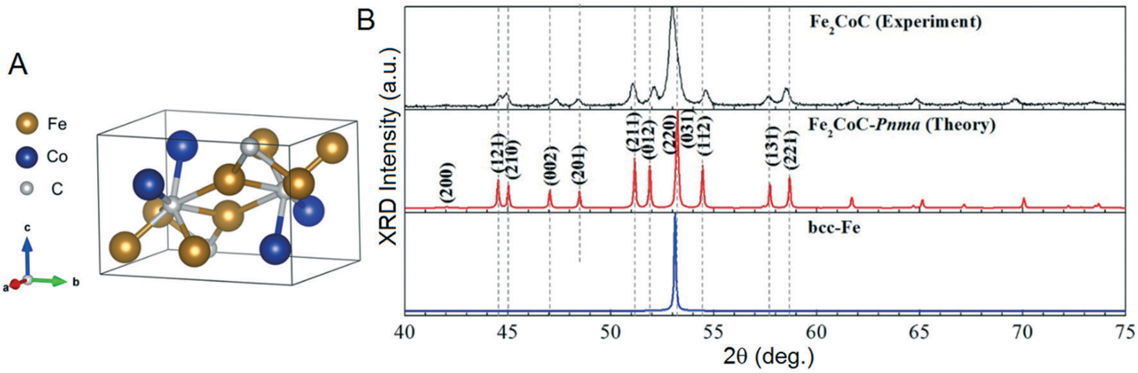

Fig. 15 Structure of Fe_2CoC. (A) Theoretically predicted unit cell for the *Pnma* phase having 4 f.u. (B) The simulated XRD pattern using the model structure is compared with the experimental XRD pattern. A simulated XRD pattern corresponding to bcc Fe is also shown for comparison (adapted from Wu *et al. J. Phys. D: Appl. Phys.* 2017, **50**, 215005).

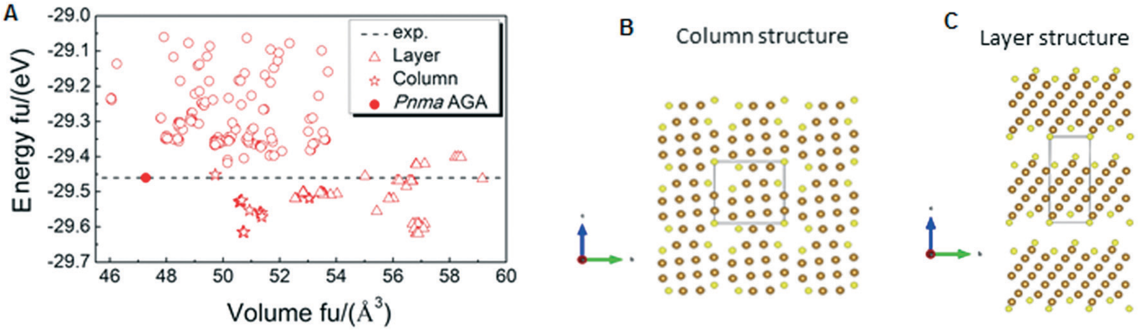

Fig. 16 Structure of Fe_3S. (A) Formation energies for various column and layered structures obtained using AGA search, where the horizontal dashed line indicates the formation energy for the *Pnma* structure obtained by experiment. Examples for the low-energy column structure (B) and layer structure (C), where the brown and yellow atoms correspond to Fe and S, respectively (adapted from Yu *et al. J Phys. D: Appl. Phys.* 2018, **51**, 075001).

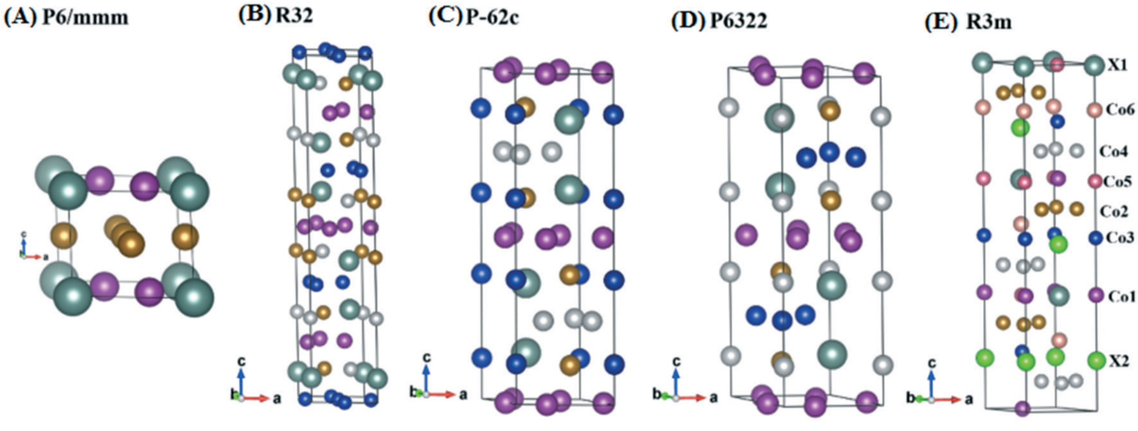

Fig. 17 Possible crystal structures for YCo_5 and $ZrCo_5$ compounds. (A) *P*6/*mmm* (space group no. 191), (B) *R*32 (no. 155), (C) $P\bar{6}2c$ (no.190), (D) $P6_322$ (no. 182), and (E) *R*3*m* (no. 160). Atomic sites labelled as X are occupied by either Y or Zr atoms. Since the Co sites are inequivalent, we categorize them in six groups, as indicated by different colors (reproduced with permission from Sakurai *et al. Phys. Rev. Mater.* 2018, **2**, 084410. Copyright (2018) by the American Physical Society).

cluster surface. For example, DFT calculations have shown ferromagnetic ordering in Mn-doped Fe–Co nanoclusters, which is rarely seen in bulk phases and the computational details can be found in the original paper.[108]

Fig. 19 shows the prototype structure of a Mn-doped Fe–Co nanocluster. From total energy calculations, the surface sites were found to be more preferable for Mn substitution. Moreover, Fe is more likely to be substituted than Co as the

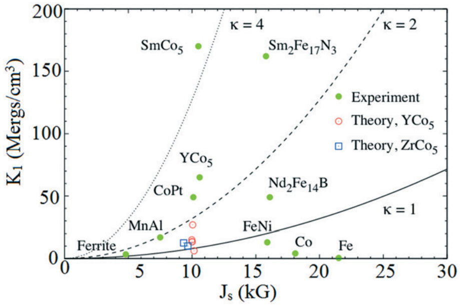

Fig. 18 Magnetic properties of YCo_5 and $ZrCo_5$. The calculated magnetocrystalline anisotropy constant K_1 *versus* the saturation magnetic polarization J_s are compared with those values of popular magnetic materials. The curves represent the magnetic hardness parameter $\kappa = (K_1/J_s^2)^{1/2}$ of 1 (solid), 2 (dashed), and 4 (dotted). Note that the present theory underestimates K_1 by a factor of about 2 (reproduced with permission from Sakurai *et al. Phys. Rev. Mater.* 2018, **2**, 084410. Copyright (2018) by the American Physical Society).

binding energy of a $MnFe_{13}Co_{14}$ cluster is larger than that of a $MnFe_{14}Co_{13}$ cluster. Using noncollinear magnetic calculations we found that surface Mn can exhibit ferromagnetic behavior similar to Fe. The ferromagnetic behavior of surface Mn is in sharp contrast to Mn bulk and Mn-based alloys, which tend to be either antiferromagnetic or paramagnetic. Surface Mn provides a larger magnetic moment to the system, whereas interior Mn, which is energetically unfavorable, does not increase the total magnetic moment.

Fig. 20 shows the evolution of the total magnetic moment for 28 atom $Mn_XFe_YCo_Z$ clusters as a function of the number of Mn dopants (X). The local magnetic moment carried by a surface Mn atom is larger than those of Fe and Co, leading to an increase of the total magnetic moment. The increase per Mn dopant is $0.9\mu_B$ ($2.9\mu_B$) per Mn atom for $Mn_XFe_{Y-X}Co_Z$ ($Mn_XFe_YCo_{Z-X}$) clusters. These results are in good agreement with the constant growth of the total magnetic moment observed in Stern–Gerlach experiments on Mn-doped transition-metal clusters.[109] Surface-Mn-induced magnetic enhancement was also observed to be robust in ternary Mn–Fe–Co clusters with different sizes and various chemical compositions.[108] The atomic positions and magnetic properties of these Mn–Fe–Co clusters can be found in the Magnetic Materials Database.[105] These theoretical findings provide a useful clue for designing new nanoclusters with a large magnetic moment.

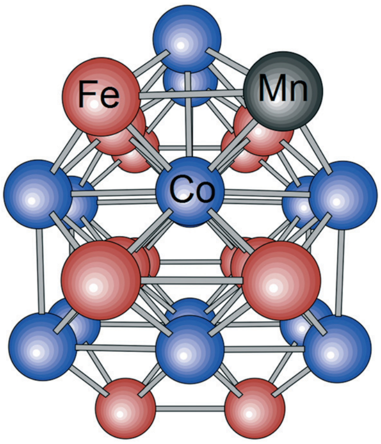

Fig. 19 $MnFe_{13}Co_{14}$ cluster. A ball-and-stick model with a body-centered cubic coordination. Fe and Co atoms are arranged in the B2-type structure (reproduced with permission from M. Sakurai and J. R. Chelikowsky, *Phys. Rev. Mater.* 2019, **3**, 044402. Copyright (2019) by the American Physical Society).

3.10. Quantum-phase-transition compounds and chiral magnetism

Quantum-phase transitions (QPTs), defined as continuous phase transitions at zero temperature, are an intriguing research topic. They are triggered by several control parameters such as mechanical pressure, magnetic or electric fields, and chemical composition.[110,111] In some solid-solution alloys of type $M_{1-x}T_x$, magnetic transition-metal elements (T) cause the nonmagnetic metal (M) to become a ferromagnet above some critical concentration x_c. An intriguing question is whether a new class of materials using QPT can be produced including novel magnetic phases that show high-temperature ferromagnetism, and compounds that exhibit chiral magnetism with room-temperature skyrmions, which may have spintronics or quantum-information applications. Two recently studied systems involving experiments and computer simulations such as $Co_{1+x}Sn$ ($0.5 \leq x \leq 1$) and $Co_{1-x}Si_{1-x}$ ($0 \leq x \leq 0.43$) are discussed below.[62,112]

CoSn with a NiAs-type hexagonal structure is a hypothetical compound, but $Co_{1+x}Sn$ compounds with $0.45 \leq x \leq 1$ and with a similar structure were produced by the rapid-quenching method.[112] On increasing x, the excess Co (x), the light blue atom in Fig. 21A, gradually enters the 2d interstitial sites and stabilizes the NiAs structure for $x \geq 0.45$. Experimental results and DFT calculations show that an excess of Co yields a Griffiths-like phase. Above a quantum critical point ($x_c \approx 0.65$), a quantum-phase transition to ferromagnetic order occurs.[112] The quantum critical behavior

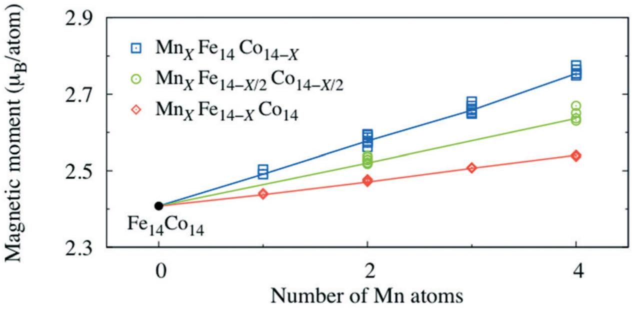

Fig. 20 Magnetism of $Mn_XFe_YCo_Z$. Total magnetic moments of 28 atom clusters as a function of the number of Mn atoms (X). The solid lines connect the values of stable isomers (reproduced with permission from M. Sakurai and J. R. Chelikowsky, *Phys. Rev. Mater.* 2019, **3**, 044402. Copyright (2019) by the American Physical Society).

on the ferromagnetic and paramagnetic sides of the transition was investigated by fitting the experimental data. Commonly used power laws for this class of materials were employed: $M_s \sim (x - x_c)^\beta$ and $\alpha \sim (x_c - x)^\zeta$, respectively, as shown in Fig. 21B. α was obtained by fitting the field-dependent magnetization on the paramagnetic side using $M \sim H^\alpha$. This analysis yields $\beta = \zeta = 0.47$ and $x_c = 0.65$. In agreement with the experimental results, the calculated density of states shows a zero net magnetic moment for $x = 0$ (Fig. 21C). Ferromagnetic ordering with an average magnetic moment of $0.52\mu_B$ per f.u (Fig. 21D) is in rough agreement with the experiment ($M_s = 0.80\mu_B$ per f.u). These QPT $Co_{1+x}Sn$ compounds also exhibit high $T_c \geq 650$ K depending on x for $0.7 \geq x \leq 1$.[112]

Magnetic compounds crystallizing in the non-centrosymmetric cubic B20 structure (space group: $P2_13$ and prototype: FeSi), as schematically shown in Fig. 22A, have recently attracted much attention as potential spin-electronics materials.[113] One of the limitations of existing B20 magnets is their low magnetic-ordering temperatures (critical temperatures) T_c of less than 300 K and this prevents their use in room-temperature applications. Some B20 alloys such as CoSi and FeSi are not even ordered at zero temperature.[113] Recently a rapid-quenching method has been used to produce B20-ordered $Co_{1+x}Si_{1-x}$ with a maximum Co solubility of $x = 0.043$.[62] The experimental results and DFT calculations reveal that the alloys are magnetically ordered above a critical excess Co content ($x_c = 0.028$), and for $x = 0.043$, a critical temperature $T_c = 328$ K was measured, the highest among all B20-ordered magnets. In support of the experimental results, the spin-up (↑) and spin-down (↓) bands are identical for $x = 0$, confirming the absence of spin polarization (Fig. 22B) and exhibit a significant difference for $x = 0.43$ (Fig. 22C), revealing magnetic ordering with a moment $0.18\mu_B$ per Co. The $Co_{1.043}Si_{0.957}$ alloy also shows a formation of skyrmions at room temperature as shown in the Lorentz TEM image (Fig. 22D). A significant aspect of this work is the small skyrmion dimensions at high temperatures ($\lambda \sim 17$ nm), which is critical for information-processing applications.[62]

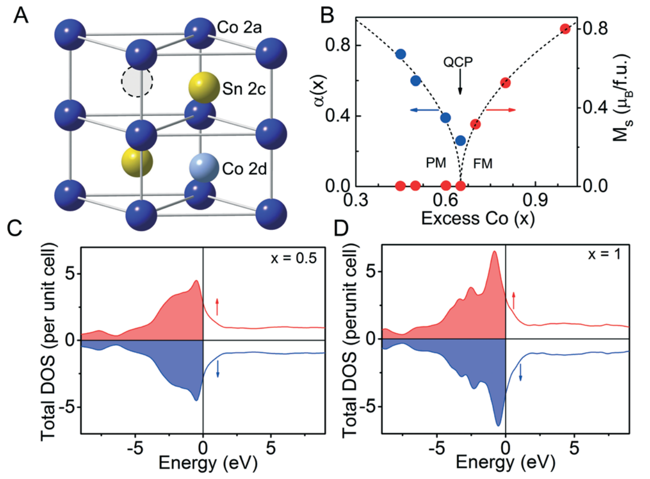

Fig. 21 Interstitially modified $Co_{1+x}Sn$ alloys. (A) Unit cell of NiAs-ordered hexagonal structure for $x = 0.5$. (B) Plots of parameters $\alpha(x)$ and $M_s(x)$ from quantum critical phase-transition analysis (see text) (adapted from Pahari *et al. Phys. Rev. B*, 2019, **99**, 184438). Total density of states: (C) $x = 0.5$ and (D) $x = 1$.

4. Prospects for new rare-earth-free magnetic materials

Most of the rare-earth-free magnetic materials discussed in this review have shown magnetocrystalline anisotropy $K_1 \geq 10$ Mergs per cm^3 (1 MJ m^{-3}) and saturation magnetic polarization $J_s \geq 10$ kG (1 T). The anisotropies of these materials are suitable to obtain a high coercivity H_c and a high energy product $(BH)_{max}$, which are essential for exploiting them for permanent-magnet applications. Note that $(BH)^{th}_{max} = J_s^2/4$ is the maximum theoretical energy product for a magnetic material, and this can be nearly achievable if the material exhibits a square M–H loop with $M_r/M_s = 1$ and $H_c \geq M_r/2$, where M_r is the remanent magnetization. The coercivity is an extrinsic property, which is determined by a combination of intrinsic magnetic properties and various nanostructural features. According to the Stoner–Wohlfarth model, the coercivity of an anisotropic (uniaxially aligned) magnetic particle or grain should be ideally equivalent to the anisotropy field, *i.e.*, $H_c = H_a = 2K_1/M_s$. H_c is also inversely proportional to M_s, which can lead to low H_c in magnetic materials with very high M_s. Therefore, a permanent-magnet material must have a sufficiently large H_a, and Hirayama *et al.* have proposed an ideal value for anisotropy field $B_a = \mu_0 H_a > 1.35\ J_s$ for a potential permanent-magnet material by taking into account various intrinsic and nanostructural details.[114]

The measured J_s and B_a values for various rare-earth-free magnetic materials are shown in Fig. 23A, where the $(BH)^{th}_{max}$ corresponding to different J_s values are also shown (top). As indicated in Fig. 23A, there are some rare-earth-free magnetic materials that exhibit $B_a > 1.35\ J_s$ and $(BH)^{th}_{max} > 25$ MGOe, which is higher than the energy product of the traditional rare-earth-free magnets such as alnico (~9.0 MGOe) and ferrites (~3.8 MGOe), and similar to the Sm–Co based rare-earth alloys (~30 MGOe).[15] Nanostructured films of $HfCo_7$ and Zr_2Co_{11} have shown maximum room-temperature energy products of about 13 MGOe and 16 MGOe, respectively (Fig. 23B).[57,58] When the easy axes of hard magnetic $HfCo_7$ and Zr_2Co_{11} phases are aligned, and combined with high-magnetization $Fe_{65}Co_{35}$ to form exchange-coupled hard–soft composite films, maximum energy products of about 20.3 MGOe were achieved at room temperature.[56,57]An optimum soft-phase addition (≤15 vol%) subsequently improved the magnetization, so the coercivity of the resultant composite films was maintained as $H_c \geq J_s/2$.[57,58]

Fig. 23C shows an energy-dispersive X-ray spectroscopy (EDS) color mapping image obtained from a high-angle annular dark-field STEM image of a $HfCo_7$: Fe–Co nanocomposite film with 7 vol% of FeCo. Such

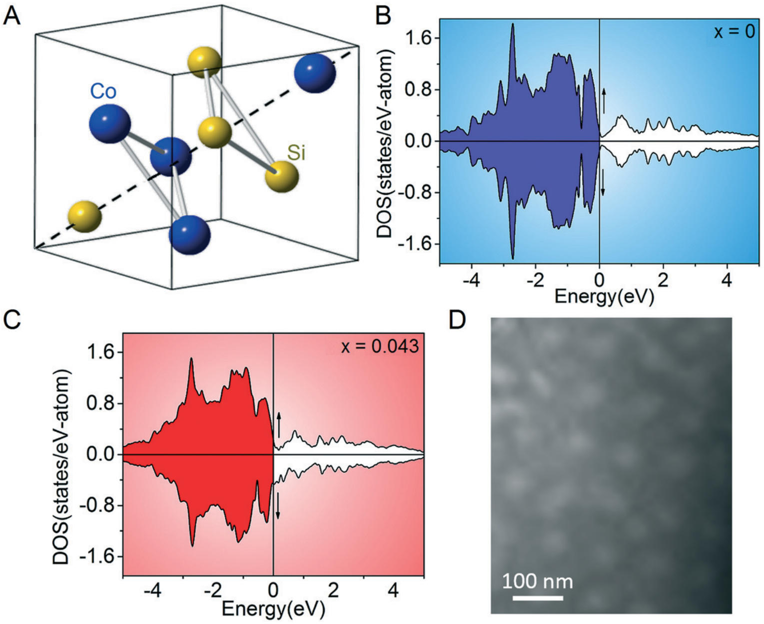

Fig. 22 Substitutional-type $Co_{1+x}Si_{1-x}$ alloys. (A) Unit cell of equiatomic CoSi. Total density of states: (B) $x = 0$ and (C) $x = 0.043$. (D) The room-temperature Lorentz TEM image for $x = 0.043$ (reproduced with permission from Balasubramanian *et al. Phys. Rev. Lett.* 2020, **124**, 057201. Copyright (2020) by the American Physical Society).

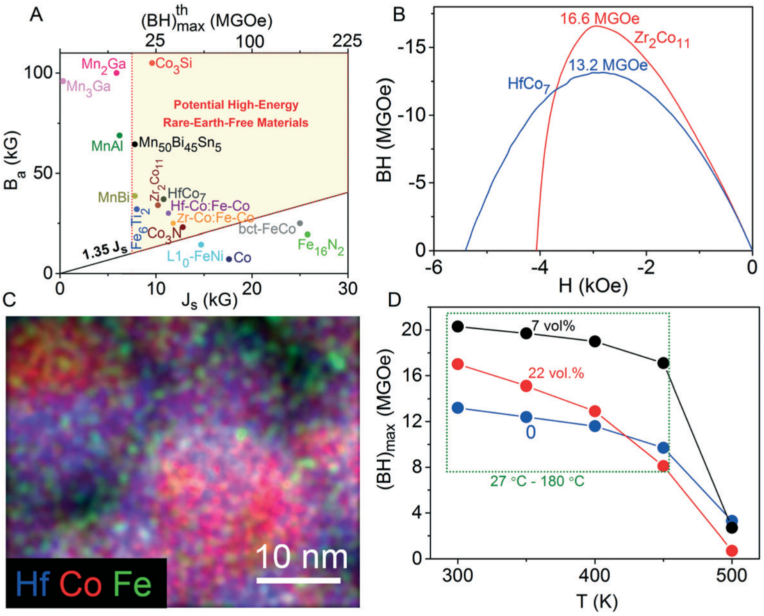

Fig. 23 Rare-earth free magnetic materials. (A) Anisotropy field ($B_a = \mu_0 H_a$) and saturation magnetic polarization (J_s). The materials in the yellow region (above 1.35 J_s) are considered as potential permanent-magnet materials. Theoretically achievable $(BH)^{th}_{max}$ corresponding to different J_s values are also plotted on the top. (B) Room-temperature (BH) curves as a function of H for the cluster-deposited nanoparticle films (data were taken from Balasubramanian *et al. Adv. Mater.* 2013, **25**, 6090 (Zr_2Co_{11}) and *Sci. Rep.* 2015, **4**, 6265 ($HfCo_7$)). Aligned exchange-coupled Hf–Co : Fe–Co nanocomposite thin films: (C) EDS color map obtained from a HAADF STEM image of a sample having Fe–Co contents of 7 vol%. (D) The measured energy products $(BH)_{max}$ as a function of temperature for different soft Fe–Co phase contents (reproduced from Balasubramanian *et al. Sci. Rep.* 2015, **4**, 6265).

nanostructured rare-earth free composite materials have also shown appreciable energy products at elevated temperatures. This is essential for permanent magnets, which often are required to operate above room temperature, for example high-performance motor applications at about 180 °C. For example, the $HfCo_7$: Fe–Co nanocomposite film with 7 vol% of Fe–Co also retain $(BH)_{max}$ values as high as 17.1 MGOe at 180 °C as shown in Fig. 23D.[58]

In the case of melt-spun samples, Hf–Co and Zr–Co alloys have shown room-temperature energy products of about 4.3 and 5.2 MGOe, respectively. Upon boron addition, this value increases to 7.7 MGOe in $Hf_{12}Co_{85}B_3$.[83] Note that these bulk alloys are isotropic (unaligned) and the energy products may be improved upon easy-axis alignment. For example, the easy-axis-aligned melt-spun MnBi ribbon sample exhibits an appreciable energy product of about 14.3 MGOe and retains it as high as about 10.8 MGOe at 200 °C.[91,94] Similarly, a maximum room-temperature energy product of 11.5 MGOe has been obtained in a compacted magnet fabricated from melt-spun ribbons having a nominal composition of $Mn_{50}Bi_{46.5}Mg_3Sb_{0.5}$.[93] These materials, and variations thereof, can be useful in applications, where magnets with energy products in the intermediate range between alnico and RE-containing magnets are required, or semi-hard applications such as data storage.

Another important aspect of new materials discussed in this review is their relevance to sustainable chemistry, green energy, and environmentally-friendly technologies. These new magnetic materials are free of critical rare-earth elements, any hazardous substance, and expensive metals such as Pt, Pd, or Au. They contain about 50–75 at% of Fe, Co, or Mn with other earth-abundant elements such as Ti, Bi, Zr, Hf, Si, S, and N. Of current geopolitical and global energy security relevance, these materials are important in developing alternative permanent-magnet materials containing only sustainable elements for clean energy and also to mitigate the supply risk of rare-earth elements. For example, the U.S. Department of Energy has developed criticality assessments for various elements using "rounded" scores by considering their importance to clean energy, and supply risk for the next 5 years.[115,116] While Nd and Dy are good for clean energy with a rounded score of 4, they are extremely critical for supply risk by showing a rounded score of 4. By comparison, Fe, Co, and Mn have been regarded as green materials for cleaner energy and possess low supply risk with a rounded score of only 2. Note that another often-used element in traditional permanent magnets, Sm, is predicted to have a comparatively lower rounded score of 1 for cleaner energy. In addition, Fe, Co, and Mn can be recycled repeatedly for multiple times and such efforts have been demonstrated successfully in the case of lithium ion batteries.[117–120]

We note that known structures of binary, ternary, and quaternary compounds available for making permanent magnets are far from being complete, *i.e.*, the number of known structures is notably less than the number of possible structures and compounds. As such, the potential for the discovery of new materials in this realm is great. However, seeking out a viable structure with desired magnetic properties is a daunting task because of a myriad of possible combinations of chemical compositions across the periodic table. A successful search using traditional "trial and error" methods would require an enormous dose of good fortune. Fortunately, a number of largely unexplored techniques exist that can guide discoveries, especially when coupled with a strong synthesis effort to work in partnership between theory as we have illustrated.

Recently, the use of artificial intelligence (AI) methods, such as machine learning, for the study of advanced materials offers a new frontier of scientific research.[121] In particular, AI-assisted materials discovery needs "big data" including massive extraction of basic knowledge from scientific literature and related databases, as well as the systematic generation of deep knowledge spaces with that information. Such inference and learning within a database space is very important to close the gap between known and hypothetical materials and decide on promising approaches, as well as to address the main issues highlighted in the strategic plan of the Materials Genome Initiative (MGI).[122]

Recently, we have been developing an open database of magnetic materials to facilitate AI-assisted materials discovery for rare-earth-free magnets within the MGI paradigm.[105] Currently, our database covers about two thousand rare-earth-free compounds; about half of them are collected from the Materials Project (MP) database and the rest are new structures from our AGA search. Detailed information about the magnetic properties including the site-specific magnetization on each atom, magnetocrystalline anisotropy energy, and Curie temperature, as well as the thermodynamic data such as the formation energy and the energy with respect to the corresponding convex hull are documented in a machine readable format.[105] The combination of these extensive datasets and advanced machine-learning techniques will enable better identification of synthesizable candidate magnets that are free of critical elements.

5. Conclusions and outlook

This article provides an overview of recently discovered Co-, Fe-, and Mn-rich magnetic materials obtained by a combined search using experiments, adaptive-genetic algorithms, and advanced electronic-structure methods. We discussed several new magnetic compounds that possess promising properties including high magnetocrystalline anisotropy, saturation magnetization, and Curie temperature. A unique approach of combining powerful computational techniques and non-equilibrium fabrication methods can be easily adapted to discover other classes of inorganic materials with desired optical, electronic, optoelectronic, dielectric and catalytic properties for significant applications.

Another important aspect of materials development is the creation of new magnetic structures by incorporating nitrogen atoms in the interstitial or substitutional occupancies of Co, Fe and Fe–Co binary alloys. The nitride compounds exhibit high magnetocrystalline anisotropies while retaining their magnetization comparable to Co and Fe. This result suggests that it might be possible to find stronger permanent-magnet materials with properties comparable to the traditional rare-earth magnets by adding nitrogen to the rare-earth-free intermetallic compounds from

Co– and/or Fe–X systems (X = N, Si, Sn, Zr, Hf, Y, C, S, Ti or Mn).

Novel rare-earth-free materials exhibit appreciable energy products up to 20.3 MGOe at room temperature and 17.1 MGOe at 180 °C in a thin-film form and about 14.3 MGOe (300 K) and 10.8 MGOe (200 °C) in the form of bulk alloys. These materials therefore can have potential uses in microelectromechanical systems (MEMS) and information-storage devices, but significant research efforts have to be initiated yet towards exploring them for the above-mentioned practical applications. Similarly, they can also be used to create future rare-earth-free permanent magnets, if scale-up methods for bulk production are developed. Such scale-up methods are essential for creating appropriate nanostructures for bulk magnetic applications, and remain a significant challenge. However, it is worth noting that rapidly-quenched MnBi-based ribbons have been used to fabricate compacted bulk magnets and demonstrated an energy product of 11.5 MGOe, higher than that of alnico magnets.[93]

Combined experimental and computational efforts also yielded new transition-metal compounds, based on Co–Sn and Co–Si near the equiatomic composition, which possess controllable quantum phase transitions, exhibit chiral magnetism with room-temperature skyrmions, and may have spintronics or quantum-information applications. It will be fruitful to investigate QPT phenomena in new compounds and determine on how Curie temperature T_c, magnetocrystalline anisotropy K_1, and helical periodicity λ can be controlled. There are several compounds similar to CoSn systems such as CoSb and FeSb,[123] which form a NiAs-type hexagonal structure with unoccupied interstitial sites. Therefore it might be possible to realize the QPT phenomenon by filling the interstitial sites of those compounds by Co or Fe and produce new materials that exhibit ferromagnetism with high T_c.

The B20-type $Co_{1+x}Si_{1-x}$ (x = 0.043) compound with magnetic ordering temperature T_c = 327 K and a skyrmion size of 17 nm is an intriguing system from the viewpoint of exploring skyrmions for practical room-temperature applications. For example, this may allow researchers to experiment with memory racetracks in nanostripes/wires and thin films at room temperature, which could transport skyrmions along the strips/films by applying an electric current. Such racetrack designs could increase processing speeds and extend the life spans of hard drives. Small skyrmions discussed in this review are advantageous for high-speed and high-density spintronics devices.[124] In addition, there are several unexplored B20-ordered compounds such as CrSi, CoGe, RuSi, RhSi, RhGe, and RhSn.[125] It is worthwhile to exploit the quantum-phase transition in these compounds by adding excess Co, which may yield new materials with high T_c and a skyrmion size below the sub-10 nm.

In brief, this review outlines a pathway for discovering new magnetic compounds with computational efficiency beyond the existing materials database, discusses the prospects of new compounds and challenges in exploring them for practical applications, and provides insights for future research to attain better efficiency and applicability. While many intriguing results have been obtained thus far, a huge amount of phase-space remains to be explored. Discoveries in this phase space will surely pay rich dividends for basic science and applications.

Conflicts of interest

There are no conflicts to declare.

Acknowledgements

This research is primarily supported by the U.S. National Science Foundation – Designing Materials to Revolutionize and Engineer our Future: Sustainable Chemistry, Engineering, and Materials (NSF-DMREF: SusChEM) under the grant numbers 1729202, 1729288, and 1729677. Research at Nebraska is also partly supported by the U.S. Department of Energy (DOE) under the award number DE-FG02-04ER46152 and performed in part in the Nebraska Nanoscale Facility: National Nanotechnology Coordinated Infrastructure and the Nebraska Center for Materials and Nanoscience, which are supported by the U.S. NSF under award NNCI-1542182, and the Nebraska Research Initiative (NRI). HPC resources were provided by the Texas Advanced Computing Center (TACC), through the Extreme Science and Engineering Discovery Environment (XSEDE) allocation, and the National Energy Research Scientific Computing Center (NERSC). The development of adaptive genetic algorithm (AGA) method was supported by the U.S DOE, Basic Energy Sciences, Division of Materials Science and Engineering, under Contract No. DE-AC02-07CH11358, including a grant of computer time at the NERSC in Berkeley, CA. We thank Xin Zhao, Manh Cuong Nguyen, Wenyong Zhang, Ralph Skomski, Haohan Wang, Shah R. Valloppilly, Xingzhong Li and Rabindra Pahari for helpful discussions.

References

1 (*a*) S. Sanvito, C. Oses, J. Xue, A. Tiwari, M. Zic, T. Archer, P. Tozman, M. Venkatesan, M. Coey and S. Curtarolo, *Sci. Adv.*, 2017, **3**, e1602241; (*b*) C. Collins, M. S. Dyer, M. J. Pitcher, G. F. S. Whitehead, M. Zanella, P. Mandal, J. B. Claridge, G. R. Darling and M. J. Rosseinsky, *Nature*, 2017, **546**, 280–284.

2 (*a*) E. M. Vogel, *Nat. Nanotechnol.*, 2007, **2**, 25–32; (*b*) J. Wood, *Mater. Today*, 2008, **11**, 40–44.

3 (*a*) K. Strnat, G. Hoffer, J. Olson and W. Ostertag, *J. Appl. Phys.*, 1967, **38**, 1001–1002; (*b*) M. Sagawa, S. Fujimura, N. Togawa, H. Yamamoto and Y. Matsuura, *J. Appl. Phys.*, 1984, **55**, 2083–2087; (*c*) M. Takahashi, H. Shoji, H. Takahashi, H. Nashi and T. Wakiyama, *J. Appl. Phys.*, 1994, **76**, 6642–6647.

4 Editorial: Fuelling discovery by sharing, *Nat. Mater.*, 2013, 12, 173.

5 J. de Pabloa, B. Jones, C. L. Kovacs, V. Ozolins and A. P. Ramirez, *Curr. Opin. Solid State Mater. Sci.*, 2014, **18**, 99.

6 O. Gutfleisch, M. A. Willard, E. Brück, C. H. Chen, S. G. Sankar and J. P. Liu, *Adv. Mater.*, 2011, **15**, 821.

7 A. Kitanovski, *Adv. Mater.*, 2020, **10**, 1903741.

8 A. Brataas, A. D. Kent and H. Ohno, *Nat. Mater.*, 2012, **11**, 372.

9 V. F. Cardoso, A. Francesko, C. Ribeiro, M. Bañobre-López, P. Martins and S. Lanceros-Mendez, *Adv. Healthcare Mater.*, 2018, **7**, 1700845.

10 L. M. Rossi, N. J. S. Costa, F. P. Silva and R. Wojcieszak, *Green Chem.*, 2014, **16**, 2906.

11 R. Skomski and J. M. D. Coey, *Permanent Magnetism*, Institute of Physics, Bristol, 1999.

12 C. A. Ross, *Annu. Rev. Mater. Res.*, 2001, **31**, 203.

13 D. Weller and M. F. Doerner, *Annu. Rev. Mater. Sci.*, 2000, **30**, 611.

14 R. Skomski and D. J. Sellmyer, *J. Rare Earths*, 2009, **27**, 675–679.

15 J. Cui, M. Kramer, L. Zhou, F. Liu, A. Gabay, G. Hadjipanayis, B. Balasubramanian and D. J. Sellmyer, *Acta Mater.*, 2018, **158**, 118.

16 N. Jones, *Nature*, 2011, **472**, 22.

17 (*a*) E. Alonso, A. M. Sherman, T. J. Wallington, M. P. Everson, F. R. Field, R. Roth and R. E. Kirchain, *Environ. Sci. Technol.*, 2012, **46**, 3406; (*b*) K. Binnemansa, P. T. Jones, B. Blanpain, T. V. Gerven, Y. Yang, A. Walton and M. Buchert, *J. Cleaner Prod.*, 2013, **51**, 1.

18 X. Zhao, S. Wu, M. C. Nguyen, K.-M. Ho and C.-Z. Wang, "Adaptive Genetic Algorithm for Structure Prediction and Application to Magnetic Materials" in *Handbook of Materials Modeling*, ed. W. Andreoni and S. Yip, Springer Nature, Switzerland AG, 2019, pp. 1–20.

19 A. Vishina, O. Y. Vekilova, T. Björkman, A. Bergman, H. C. Herper and O. Eriksson, *Phys. Rev. B*, 2020, **101**, 094407.

20 D. J. Sellmyer, B. Balamurugan, B. Das, P. Mukherjee, R. Skomski and G. C. Hadjipanayis, *J. Appl. Phys.*, 2015, **117**, 172609.

21 B. Balamurugan, B. Das, W. Y. Zhang, R. Skomski and D. J. Sellmyer, *J. Phys. Condens. Matter*, 2014, **26**, 064204.

22 S. Q. Wu, M. Ji, C. Z. Wang, M. C. Nguyen, X. Zhao, K. Umemoto, R. M. Wentzcovitch and K. M. Ho, *J. Phys.: Condens. Matter*, 2014, **26**, 035402.

23 X. Zhao, Q. Shu, M. C. Nguyen, Y. Wang, M. Ji, H. Xiang, K. M. Ho, X. Gong and C. Z. Wang, *J. Phys. Chem. C*, 2014, **118**, 9524.

24 D. M. Deaven and K. M. Ho, *Phys. Rev. Lett.*, 1995, **75**, 288.

25 K. M. Ho, A. Shvartsburg, B. C. Pan, Z. Y. Lu, C. Z. Wang, J. Wacker, J. L. Fye and M. F. Jarrold, *Nature*, 1998, **392**, 582.

26 F. C. Chuang, C. Z. Wang and K. M. Ho, *Phys. Rev. B: Condens. Matter Mater. Phys.*, 2006, **73**, 125431.

27 T. L. Chan, C. V. Ciobanu, F.-C. Chuang, N. Lu, C. Z. Wang and K. M. Ho, *Nano Lett.*, 2006, **6**, 277.

28 J. Zhang, C. Z. Wang and K. M. Ho, *Phys. Rev. B: Condens. Matter Mater. Phys.*, 2009, **80**, 174102.

29 A. O. Lyakhov, A. R. Oganov, H. Stokes and Q. Zhu, *Comput. Phys. Commun.*, 2013, **184**, 1172.

30 M. Ji, K. Umemoto, C. Z. Wang, K. M. Ho and R. M. Wentzcovitch, *Phys. Rev. B: Condens. Matter Mater. Phys.*, 2011, **84**, 220105(R).

31 S. Q. Wu, K. Umemoto, M. Ji, C. Z. Wang, K. M. Ho and R. M. Wentzcovitch, *Phys. Rev. B: Condens. Matter Mater. Phys.*, 2011, **83**, 184102.

32 M. C. Nguyen, J. H. Choi, X. Zhao, C. Z. Wang, Z. Zhang and K. M. Ho, *Phys. Rev. Lett.*, 2013, **111**, 165502.

33 X. Zhao, M. C. Nguyen, C. Z. Wang and K. M. Ho, *J. Phys.: Condens. Matter*, 2014, **26**, 455401.

34 M. S. Daw and M. I. Baskes, *Phys. Rev. B: Condens. Matter Mater. Phys.*, 1984, **29**, 6443.

35 P. Brommer and F. Gahler, *Modell. Simul. Mater. Sci. Eng.*, 2007, **15**, 295.

36 P. Brommer and F. Gahler, *Philos. Mag.*, 2006, **86**, 753.

37 P. Hohenberg and W. Kohn, *Phys. Rev.*, 1964, **136**, B864.

38 W. Kohn and L. J. Sham, *Phys. Rev.*, 1965, **140**, A1133.

39 M. C. Payne, M. P. Teter, D. C. Allan, T. A. Arias and J. D. Joannopoulos, *Rev. Mod. Phys.*, 1992, **64**, 1045.

40 J. P. Perdew, K. Burke and M. Ernzerhof, *Phys. Rev. Lett.*, 1996, **77**, 3865.

41 L. Frediani and D. Sundholm, *Phys. Chem. Chem. Phys.*, 2015, **17**, 31357.

42 (*a*) J. R. Chelikowsky, N. Troullier and Y. Saad, *Phys. Rev. Lett.*, 1994, **72**, 1240; (*b*) J. R. Chelikowsky, N. Troullier, K. Wu and Y. Saad, *Phys. Rev. B: Condens. Matter Mater. Phys.*, 1994, **50**, 11355.

43 L. Kronik, A. Makmal, M. L. Tiago, M. M. G. Alemany, M. Jain, X. Huang, Y. Saad and J. R. Chelikowsky, *Phys. Status Solidi B*, 2006, **243**, 1063.

44 J. Souto-Casares, M. Sakurai and J. R. Chelikowsky, *Phys. Rev. B*, 2016, **93**, 174418.

45 M. Sakurai, J. Souto-Casares and J. R. Chelikowsky, *Phys. Rev. B*, 2016, **94**, 024437.

46 M. Sakurai, X. Zhao, C.-Z. Wang, K.-M. Ho and J. R. Chelikowsky, *Phys. Rev. Mater.*, 2018, **2**, 024401.

47 Y. Zhou, Y. Saad, M. L. Tiago and J. R. Chelikowsky, *Phys. Rev. E*, 2006, **74**, 066704.

48 Y. Zhou, Y. Saad, M. L. Tiago and J. R. Chelikowsky, *J. Comput. Phys.*, 2006, **219**, 172.

49 Y. Zhou, J. R. Chelikowsky and Y. Saad, *J. Comput. Phys.*, 2014, **274**, 770.

50 A. K. Rajagopal and J. Callaway, *Phys. Rev. B: Solid State*, 1973, **7**, 1912.

51 A. H. MacDonald and S. H. Vosko, *J. Phys. C: Solid State Phys.*, 1979, **12**, 2977.

52 D. Naveh and L. Kronik, *Solid State Commun.*, 2009, **149**, 177.

53 M. Sakurai and J. R. Chelikowsky, *Phys. Rev. Mater.*, 2018, **2**, 084411.

54 B. Balasubramanian, K. L. Kraemer, N. A. Reding, R. Skomski, S. Ducharme and D. J. Sellmyer, *ACS Nano*, 2010, **4**, 1893.

55 B. Balasubramanian, X. Zhao, S. R. Valloppilly, S. Beniwal, R. Skomski, A. Sarella, Y. Jin, X. Z. Li, X. Xu, H. Cao, H. Wang, A. Enders, C.-Z. Wang, K.-M. Ho and D. J. Sellmyer, *Nanoscale*, 2018, **10**, 13011.

56 B. Balamurugan, B. Das, V. R. Shah, R. Skomski, X. Z. Li and D. J. Sellmyer, *Appl. Phys. Lett.*, 2012, **101**, 122407.

57 B. Balasubramanian, B. Das, R. Skomski, W. Zhang and D. J. Sellmyer, *Adv. Mater.*, 2013, **25**, 6090.

58 B. Balasubramanian, P. Mukherjee, R. Skomski, P. Manchanda, B. Das and D. J. Sellmyer, *Sci. Rep.*, 2015, **4**, 6265.

59 B. Balasubramanian, P. Manchanda, R. Skomski, P. Mukherjee, S. R. Valloppilly, B. Das, G. C. Hadjipanayis and D. J. Sellmyer, *Appl. Phys. Lett.*, 2016, **108**, 152406.

60 H. Okamoto, *Phase Diagram of Binary Alloys*, ASM, Materials Park, Ohio, 2000, p. 259.

61 (*a*) K. Ishida and T. Nishizawa, *J. Phase Equilib.*, 1991, **12**, 578; (*b*) ICDD, International Centre for Diffraction Data, Card No. 04-001-3215, 2014.

62 B. Balasubramanian, P. Manchanda, R. Pahari, Z. Chen, W. Zhang, S. R. Valloppilly, X. Li, A. Sarella, L. Yue, A. Ullah, P. Dev, D. A. Muller, R. Skomski, G. C. Hadjipanayis and D. J. Sellmyer, *Phys. Rev. Lett.*, 2020, **124**, 057201.

63 X. Zhao, L. Ke, C.-Z. Wang and K.-M. Ho, *Phys. Chem. Chem. Phys.*, 2016, **18**, 31680.

64 H. Okamoto, *Phase Diagram of Binary Alloys*, ASM, Materials Park, Ohio, 2000, p. 252.

65 M. Widenmyer, L. Shlyk, N. Becker, R. Dronskowski, E. Meissner and R. Niewa, *Eur. J. Inorg. Chem.*, 2016, **2016**, 4792.

66 M. B. Lourenco, M. D. Carvalho, P. Fonseca, T. Gasche, G. Evans and M. Godinho, *J. Alloys Compd.*, 2014, **612**, 176.

67 K. Suzuki, T. Kaneko, H. Yoshida, H. Morita and H. Fujimori, *J. Alloys Compd.*, 1995, **224**, 232.

68 B. C. Sales, B. Saparov, M. A. McGuire, D. J. Sing and D. S. Parker, *Sci. Rep.*, 2014, **4**, 7024.

69 X. Zhao, S. Yu, S. Wu, M. C. Nguyen, C.-Z. Wang and K.-M. Ho, *Phys. Rev. B*, 2017, **96**, 024422.

70 J. Fischbacher, A. Kovacs, H. Oezelt, M. Gusenbauer, D. Suess and T. Schrefl, *Appl. Phys. Lett.*, 2017, **111**, 192407.

71 O. Y. Vekilova, B. Fayyazi, K. P. Skokov, O. Gutfleisch, C. Echevarria-Bonet, J. M. Barandiarán, A. Kovacs, J. Fischbacher, T. Schrefl, O. Eriksson and H. C. Herper, *Phys. Rev. B*, 2019, **99**, 024421.

72 J. Zhang, M. C. Nguyen, B. Balasubramanian, B. Das, D. J. Sellmyer, Z. Zeng, K.-M. Ho and C.-Z. Wang, *J. Phys. D: Appl. Phys.*, 2016, **49**, 175002.

73 B. Balasubramanian, B. Das, M. C. Nguyen, X. Xu, J. Zhang, X. Zhang, Y. Liu, A. Huq, S. R. Valloppilly, Y. Jin, C.-Z. Wang, K.-M. Ho and D. J. Sellmyer, *APL Mater*, 2016, **4**, 116109.

74 X. Xu, X. Zhang, Y. Yin, B. Balasubramanian, B. Das, Y. Liu, A. Huq and D. J. Sellmyer, *J. Phys. D: Appl. Phys.*, 2017, **50**, 025002.

75 H. Wang, B. Balasubramanian, R. Pahari, B. R. Skomski, Y. Liu, A. Huq, D. J. Sellmyer and X. Xu, *Phys. Rev. Mater.*, 2019, **3**, 064403.

76 (*a*) B. G. Demczyk and S. F. Cheng, *J. Appl. Crystallogr.*, 1991, **24**, 1023; (*b*) A. M. Gabay, Y. Zhang and G. C. Hadjipanayis, *J. Magn. Magn. Mater.*, 2001, **236**, 37.

77 (*a*) G. V. Ivanova, N. N. Shchegoleva and A. M. Gabay, *J. Alloys Compd.*, 2007, **432**, 135; (*b*) G. V. Ivanova and N. N. Shchegoleva, *Phys. Met. Metallogr.*, 2009, **107**, 270.

78 X. Zhao, M. C. Nguyen, W. Y. Zhang, C. Z. Wang, M. J. Kramer, D. J. Sellmyer, X. Z. Li, F. Zhang, L. Q. Ke, V. P. Antropov and K.-M. Ho, *Phys. Rev. Lett.*, 2014, **112**, 045502.

79 B. Das, B. Balamurugan, P. Kumar, R. Skomski, V. R. Shah, J. E. Shield, A. Kashyap and D. J. Sellmyer, *IEEE Trans. Magn.*, 2013, **49**, 3215.

80 M. C. Nguyen, L. Ke, X. Zhao, V. Antropov, C.-Z. Wang and K.-M. Ho, *IEEE Trans. Magn.*, 2013, **49**, 3281.

81 M. A. McGuire and R. Orlando, *J. Appl. Phys.*, 2015, **117**, 053912.

82 M. A. McGuire, O. Rios, N. J. Ghimire and M. Koehler, *Appl. Phys. Lett.*, 2012, **101**, 202401.

83 H. W. Chang, M. C. Liao, C. W. Shih, W. C. Chang, C. C. Yang, C. H. Hsiao and H. Ouyang, *Appl. Phys. Lett.*, 2014, **105**, 192404.

84 L. Y. Chen, H. W. Chang, C. H. Chiu, C. W. Chang and W. C. Chang, *J. Appl. Phys.*, 2005, **97**, 10F307.

85 Y. Jin, W. Zhang, P. R. Kharel, S. R. Valloppilly, R. Skomski and D. J. Sellmyer, *AIP Adv.*, 2016, **6**, 056002.

86 T. Ishikawa and K. Ohmori, *IEEE Trans. Magn.*, 1990, **26**, 1370–1372.

87 R. Skomski, *J. Phys.: Condens. Matter*, 2003, **15**, R841.

88 J. B. Yang, Y. B. Yang, X. G. Chen, X. B. Ma, J. Z. Han, Y. C. Yang, S. Guo, A. R. Yan, Q. Z. Huang, M. M. Wu and D. F. Chen, *Appl. Phys. Lett.*, 2011, **99**, 082505.

89 J. Cui, J.-P. Choi, G. Li, E. Polikarpov, J. Darsell, N. Overman, M. Olszta, D. Schreiber, M. Bowden, T. Droubay, M. J. Kramer, N. A. Zarkevich, L. L. Wang, D. D. Johnson, M. Marinescu, I. Takeuchi, Q. Z. Huang, H. Wu, H. Reeve, N. V. Vuong and J. Ping Liu, *J. Phys.: Condens. Matter*, 2014, **6**, 064212.

90 A. Sakuma, Y. Manabe and Y. Kota, *J. Phys. Soc. Jpn.*, 2013, **82**, 073704.

91 W. Zhang, R. Skomski, P. R. Kharel, L. Yue and D. J. Sellmyer, *2019 Joint MMM-Intermag Conference, Book of Abstracts*, Washington, DC, January 14–18, 2019, p. 480.

92 A. M. Gabay, G. C. Hadjipanayis and J. Cui, *J. Alloys Compd.*, 2019, **792**, 77.

93 A. M. Gabay, G. C. Hadjipanayis and J. Cui, *J. Magn. Magn. Mater.*, 2020, **495**, 165860.

94 W. Zhang, B. Balasubramanian, P. Kharel, R. Pahari, S. R. Valloppilly, X. Z. Li, L. Yue, R. Skomski and D. J. Sellmyer, *APL Mater.*, 2019, **7**, 121111.

95 X. Zhao, C. Z. Wang, Y. X. Yao and K. M. Ho, *Phys. Rev. B*, 2016, **94**, 224424.

96 D. Odkhuu and S. C. Hong, *Phys. Rev. B*, 2019, **11**, 054085.

97 (*a*) V. G. Harris, Y. Chen, A. Yang, S. Yoon, Z. Chen, A. L. Geiler, J. Gao, C. N. Chinnasamy, L. H. Lewis and C. Vittoria, *J. Phys. D: Appl. Phys.*, 2010, **43**, 165003; (*b*) Y. Zhang, G. S. Chaubey, C. Rong, Y. Ding, P. Narayan, P. Tsai,

Q. Zhang and J. P. Liu, *J. Magn. Magn. Mater.*, 2011, **323**, 1495.
98 A. A. El-Gendy, M. Bertino, D. Clifford, M. Qian, S. N. Khanna and E. E. Carpenter, *Appl. Phys. Lett.*, 2015, **106**, 213109.
99 S. Q. Wu, B. Balasubramanian, M. C. Nguyen, X. Zhao, C. Z. Wang, D. J. Sellmyer and K.-M. Ho, *J. Phys. D: Appl. Phys.*, 2017, **50**, 215005.
100 S. Yu, S. Q. Wu, M. C. Nguyen, X. Zhao, Z. Z. Zhu, C. Z. Wang and K.-M. Ho, *J. Phys. D: Appl. Phys.*, 2018, **51**, 075001.
101 M. Sakurai, S. Wu, X. Zhao, M. C. Nguyen, C.-Z. Wang, K.-M. Ho and J. R. Chelikowsky, *Phys. Rev. Mater.*, 2018, **2**, 084410.
102 A. Jain, S. P. Ong, G. Hautier, W. Chen, W. D. Richards, S. Dacek, S. Cholia, D. Gunter, D. Skinner, G. Ceder and K. A. Persson, *APL Mater.*, 2013, **1**, 011002.
103 W. Y. Zhang, X. Z. Li, S. Valloppilly, R. Skomski, J. E. Shield and D. J. Sellmyer, *J. Phys. D: Appl. Phys.*, 2013, **46**, 135004.
104 Z. Ye, F. Zhang, Y. Sun, M. I. Mendelev, R. T. Ott, E. Park, M. F. Besser, M. J. Kramer, Z. Ding, C.-Z. Wang and K.-M. Ho, *Appl. Phys. Lett.*, 2015, **106**, 101903.
105 Visit https://magmatdb.herokuapp.com/ for Magnetic Materials Database.
106 B. Balasubramanian, P. Manchanda, R. Skomski, P. Mukherjee, B. Das, T. A. George, G. C. Hadjipanayis and D. J. Sellmyer, *Appl. Phys. Lett.*, 2015, **106**, 242401.
107 M. Billas, A. Châtelain and W. A. de Heer, *Science*, 1994, **265**, 1682.
108 M. Sakurai and J. R. Chelikowsky, *Phys. Rev. Mater.*, 2019, **3**, 044402.
109 S. Yin, R. Moro, X. Xu and W. A. de Heer, *Phys. Rev. Lett.*, 2007, **98**, 113401.
110 M. Brando, D. Belitz, F. M. Grosche and T. R. Kirkpatrick, *Rev. Mod. Phys.*, 2016, **88**, 025006.
111 T. Vojta, *Annu. Rev. Condens. Matter Phys.*, 2019, **10**, 233.
112 R. Pahari, B. Balasubramanian, R. Pathak, M. C. Nguyen, S. R. Valloppilly, R. Skomski, A. Kashyap, C.-Z. Wang, K.-M. Ho, G. C. Hadjipanayis and D. J. Sellmyer, *Phys. Rev. B*, 2019, **99**, 184438.
113 N. Nagaosa and Y. Tokura, *Nat. Nanotechnol.*, 2013, **8**, 899.
114 Y. Hirayama, T. Miyake and K. Hono, *JOM*, 2015, **67**, 1344.
115 https://www.energy.gov/sites/prod/files/edg/news/documents/criticalmaterialsstrategy.pdf.
116 http://css.umich.edu/sites/default/files/Critical%20Materials_CSS14-15_e2019.pdf.
117 G. Harper, *et al.*, *Nature*, 2019, **575**, 75.
118 W. Lv, Z. Wang, H. Cao, Y. Sun, Y. Zhang and Z. Sun, *ACS Sustainable Chem. Eng.*, 2018, **6**, 1504.
119 X. Zhang, *et al.*, *Chem. Soc. Rev.*, 2018, **47**, 7239.
120 S. Ghosh, S. Mohanty, A. Akcil, L. B. Sukla and A. P. Das, *Chemosphere*, 2016, **154**, 628–639.
121 K. T. Butler, D. W. Davies, H. Cartwright, O. Isayev and A. Walsh, *Nature*, 2018, **559**, 547.
122 Materials Genome Initiative Strategic Plan, http://www.nist.gov/mgi/upload/MGI-StrategicPlan-2014.pdf.
123 H. Okamoto, *Phase Diagram of Binary Alloys*, ASM, Materials Park, 2000, pp. 258.
124 L. Caretta, *et al.*, *Nat. Nanotechnol.*, 2018, **13**, 1154.
125 D. A. Pshenay-Severin and A. T. Burkov, *Materials*, 2019, **12**, 2710.